Ultracold Surface Collisions: Sticking Probability of Atomic Hydrogen on Superfluid ^{4}He

by

Ite Albert Yu

Submitted to the Department of Physics
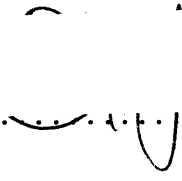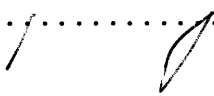in partial fulfillment of the requirements for the degree of
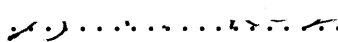
Doctor of Philosophy

at the

MASSACHUSETTS INSTITUTE OF TECHNOLOGY

September 1993

Author . . . .
Department of Physics
August 25, 1993

Certified by . . . .
Thomas J. Greytak
Professor of Physics
Thesis Supervisor

Accepted by . . . .
George F. Koster
Chairman, Department of Physics Graduate Committee

Ultracold Surface Collisions: Sticking Probability of Atomic Hydrogen on Superfluid ^{4}He

by

Ite Albert Yu

Submitted to the Department of Physics
on August 25, 1993, in partial fulfillment of the
requirements for the degree of
Doctor of Philosophy

Abstract

The sticking probability of atomic hydrogen on superfluid ^{4}He has been measured for atom temperatures between 300 μK and 4 mK. Data are presented for a superfluid ^{4}He film at 85 mK on a sintered silver substrate with film thickness varied from 0.5 nm to a bulk puddle. The results of the sticking probability measurements for bulk ^{4}He provide the first experimental evidence for universal quantum reflection and are in good agreement with recent theories. The observed film thickness dependence of the sticking probability clearly demonstrates the influence of the van der Waals-Casimir force due to the substrate.

Thesis Supervisor: Thomas J. Greytak
Title: Professor of Physics

Acknowledgments

It has been unforgettable six years for my study in M. I. T. This would not be possible without the support and the patience of Professor Thomas Greytak and Professor Daniel Kleppner. I am grateful for all their help.

John Doyle, Jon Sandberg, Claudio Cesar, Mike Yoo, Adam Polcyn, and Dale Fried are excellent friends and colleagues. I am very lucky to work with them and I appreciate the wonderful experiences that they have provided. They have great influence on me and I hope I have returned something good to them.

I thank Fu-Shu Jeng family, Jin-Yuan Liu family, Cliff Cheng, Shun-Min Lee family, Nai-Hsin Ting, Naoto Masuhara, Peggy Berkovitz, Janet Sahlstrom, and members of 8th R. O. C. S. A. executive board. They make me feel warm and pleasant. My final gratitude goes to my wife, Tsai-Ling Tang. She is always there for me.

To my wife

Contents

List of Figures

Chapter 1

Introduction

Atom-surface collisions explore interesting physics from the point of view of fundamental theory as well as practical applications. The collision can study surface structures and inter-atomic interactions. They also present well-defined and important quantum many-body problems. The work presented here tests the fundamental concept of universal quantum reflection and explores long-range inter-atomic forces by measuring the sticking probability of ultracold atomic hydrogen on a superfluid ^{4}He covered surface.

In this chapter, surface sticking theories are briefly described. The latest theoretical and experimental results concerning the sticking probability of atomic hydrogen on liquid ^{4}He are also reviewed. The findings of this work and the outline of the rest of the thesis are presented at the end of this chapter.

1.1 Theory of Surface Sticking

The sticking probability, $s(E_\perp)$, of a particle on a surface is the transition probability from continuum states to bound states of the particle-surface interaction potential normalized to unit incident flux, where $E_\perp$ is the energy of the incoming particle associated with the motion perpendicular to the surface. Various theories have been predicted different values for $s(E_\perp=0)$. A classical analysis claims $s(0)$ should always
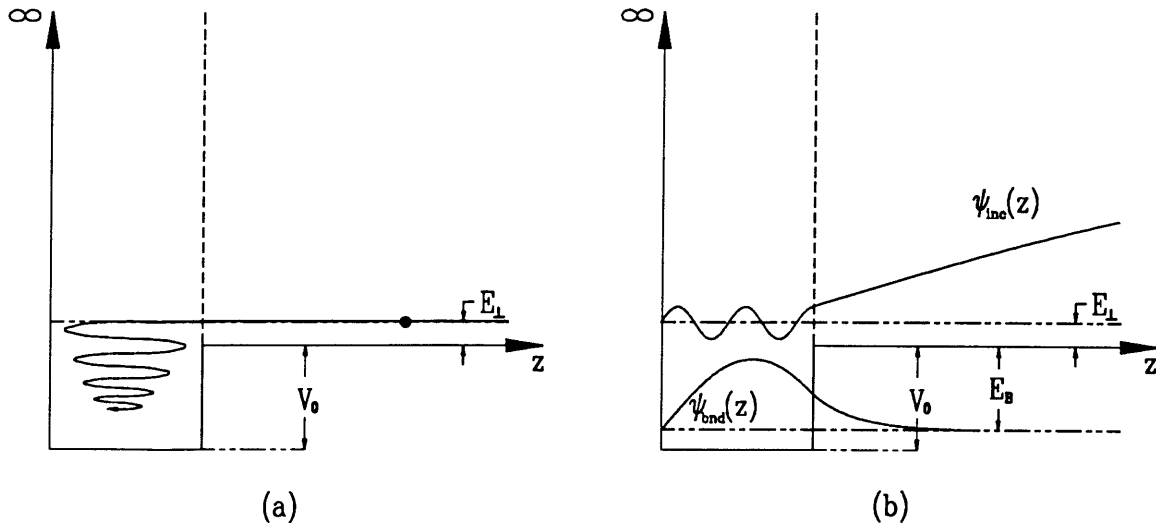
Figure 1-1: Simple description of surface sticking. (a) classical model; (b) quantum model.

go to unity [1]. A quantum analysis could predict that $s(0)$ is zero [2, 3] or even a value between 0 and 1 [4, 5] depending on the strength and nature of the interaction. This fundamental question is still unresolved.

Simple descriptions of surface sticking theory in both classical and quantum models are described in this section. As a result of a simplified quantum model, universal quantum reflection is predicted. A popular quantum approach to this problem by distorted-wave Born approximation is also presented.

1.1.1 Simple Descriptions of Classical Adsorption and Quantum Reflection

Consider a simplified one-dimension particle-surface potential well and an incident particle with energy $E_\perp$ as shown in Figure 1-1. The potential well has a finite length with depth V_0 ($\gg E_\perp$) and an infinite barrier at $z = 0$. In Figure 1-1 (a), the incident particle is a classical point-like particle. As $E_\perp \to 0$, any finite excitation of the surface by the particle inside the potential well dissipates the energy of the incoming particle and, therefore, causes the particle to become trapped. Thus $s(0) \to 1$ for classical

11

adsorption. The adsorption could be caused by the coupling between surface waves (ripplons) and the particle, or more exotic mechanisms. Quantum mechanically, the incident particle is represented by a quantum wave function, $\psi_{inc}(z)$, as in Figure 1-1 (b). In order to match the incoming wave function at the boundary of the potential, the amplitude of the wave function inside the potential well, A_{in}, is reduced by

$$A_{in} \propto A_{out}\sqrt{E_\perp/V_0} \quad (\text{as } E_\perp \to 0) \tag{1.1}$$

where A_{out} is the amplitude of the incoming wave function outside the potential well. According to the definition of the sticking probability,

$$
\begin{aligned}
s(E_\perp) &\propto |\langle\psi_{bnd}| H_{int} |\psi_{inc}\rangle|^2 /(\text{flux of incoming particle}) \\
&\propto |\langle\psi_{bnd}| H_{int} |\psi_{inc}\rangle|^2 /(A_{out}^2 v_{inc})
\end{aligned}
\tag{1.2}
$$

where $|\psi_{bnd}\rangle$ is the bound state of the potential, H_{int} is the coupling Hamiltonian, and $v_{inc}(\propto \sqrt{E_\perp})$ is the velocity of the incoming particle. Since the bound state is localized inside the potential well, the numerator of the above equation is just proportional to A_{in}^2. Substituting A_{in} by $A_{out}\sqrt{E_\perp/V_0}$,

$$s(E_\perp) \propto A_{in}^2/(A_{out}^2\sqrt{E_\perp}) = \sqrt{E_\perp}/V_0 \tag{1.3}$$

Therefore, $s(E_\perp) \propto \sqrt{E_\perp}$ as $E_\perp \to 0$ or $s(T) \propto \sqrt{T}$ as $T \to 0$ for a Boltzmann gas at temperature T. This is quantum reflection.

The predictions of these simplified classical and quantum models are quite different. The classical result has been shown to be exact [1]. The quantum result is only true under certain (perhaps, most) circumstances. A long-range potential or strong coupling could invalid the phase coherence argument of the quantum model [2, 5]. In spite of its apparent universality— independent of incoming atom and surface material— the limiting form $s(E_\perp) \propto \sqrt{E_\perp}$ or $s(T) \propto \sqrt{T}$ has never been observed experimentally in any system.

1.1.2 Distorted-Wave Born Approximation

The distorted-wave Born approximation (DWBA) provides an analytic version of the simple quantum model presented above. Consider a hydrogen atom interacting with a liquid ^{4}He surface through an interaction potential $V(z)$, which supports only one bound state with binding energy $E_B \approx 1$ K. The "distorted" wave function for the incident hydrogen atom, with energy $\hbar^2(k_\parallel^2 + k_\perp^2)/2m \equiv E_\parallel + E_\perp$, can be written as $\langle x, y \mid k_\parallel \rangle \langle z \mid k_\perp \rangle$. $\langle x, y \mid k_\parallel \rangle$ is a two dimensional free particle wave function and $\langle z \mid k_\perp \rangle$ is the solution of the following one dimensional Schrödinger equation

$$[-\frac{\hbar^2}{2m}\frac{d^2}{dz^2} + V(z)]\langle z \mid k_\perp \rangle = E_\perp \langle z \mid k_\perp \rangle \ . \tag{1.4}$$

By following Fermi's golden rule, the sticking probability is given by

$$s(E_\perp) = \frac{2\pi}{\hbar} \sum_q |\langle n(q)+1, k_\parallel', B| H_{int} |n(q), k_\parallel, k_\perp \rangle|^2 \ \delta[E_\parallel + E_\perp - E_\parallel' - E_B - \epsilon_q] +$$

$$|\langle n(q)-1, k_\parallel', B| H_{int} |n(q), k_\parallel, k_\perp \rangle|^2 \ \delta[E_\parallel + E_\perp - E_\parallel' - E_B + \epsilon_q] \ . \tag{1.5}$$

where the first and the second terms in the summation correspond to the creation and the annihilation of a ripplon respectively. Furthermore, $n(q)$ is the ripplon population number and ϵ_q is the ripplon energy, while q is a two dimensional wave vector on the surface. $\langle z \mid B \rangle$ is the wave function for the only bound state of $V(z)$ and has binding energy E_B. $\langle x, y \mid k_\parallel' \rangle$ is the wave function of a particle moving along on the ^{4}He surface with energy $E_\parallel'(= \hbar^2 k_\parallel'^2/2m)$. In order to conserve momentum, $k_\parallel' = k_\parallel \mp q$ depending on whether a ripplon is created or annihilated. Finally, H_{int} is the particle-ripplon coupling Hamiltonian determined from the microscopic interaction between the hydrogen atom and the sinusoidally distorted ^{4}He surface. It will not be discussed here.

The ripplon dispersion relation of liquid ^{4}He is $\epsilon_q = \hbar\sqrt{gq + (\gamma/\rho_0)q^3}$, where $\gamma = 0.378$ erg/cm^2 is the ^{4}He surface tension, ρ_0 is the liquid ^{4}He density, and g is the sum of the gravitational acceleration and the van der Waals force per unit mass due to the substrate underneath liquid ^{4}He. In order to conserve both energy

13

and momentum, a 0.6-K ripplon is created or a 3.5-K ripplon is annihilated when a hydrogen atom with an incident energy much less than 1 K (the binding energy) is adsorbed on the surface. For a 0.6-K or 3.5-K ripplon, the gq term in the ripplon dispersion relation is negligible. The thermal populations of 0.6-K and 3.5-K ripplons can also be neglected in $s(E_\perp)$ calculations, as long as the surface temperature is below 100 mK. Therefore, the sticking probability at surface temperatures below 100 mK is approximately the same as that at zero surface temperature and the ripplon-annihilation term in Equation 1.5 can be neglected at these surface temperatures.

Theories [6, 7, 8, 9, 10, 11] based on the above approach all predict that the sticking probability of atomic hydrogen on liquid ^{4}He in the low energy limit should be proportional to $\sqrt{E_\perp}$. The constant of proportionality differs considerably, however, from calculation to calculation. Although the nature of the interaction may require that the calculations be extended beyond the DWBA [10, 11], the hydrogen-helium surface problem is not expected to lead to a situation where $s(0) \neq 0$.

1.2 Review of Hydrogen-Liquid ^{4}He Collision

Hydrogen-liquid ^{4}He makes an ideal system for surface sticking studies. Hydrogen is the simplest atom and liquid helium provides the weakest van der Waals force of any condensed medium. The interaction potential between the hydrogen atom and the liquid ^{4}He supports only one bound state with $E_B \approx 1$ K. Furthermore, the surface excitation (ripplon) of liquid ^{4}He is well understood and the high purity of liquid ^{4}He prevents surface imperfections. Because of these features, many calculations [6, 7, 8, 9, 10, 11] have been done for this system. They all predict quantum reflection behavior in the limit of low energies.

Only recently has the development of cold atomic hydrogen sources made experimental studies of this system possible. However, data of Berkhout et al. [12, 13] at 145 mK $< T <$ 526 mK and data of Helffrich et al. [14, 15] at 0.1 K $< T <$ 0.4 K showed a linear dependence of the sticking probability on temperature. This indicated that the low energy limit had not been reached at these temperatures. Using evaporative

cooling to produce submillikelvin atomic hydrogen, Doyle et al. [16] reported that the sticking probability for 100 μK $< E_\perp <$ 10 mK had a relatively high value and slightly increased with decreasing atom energy. These surprising results prompted Hijmans et al. [9] to propose that the substrate underneath a liquid ^{4}He film was playing a role. Calculations of Hijmans et al. [9], and Carraro and Cole [10, 11] indicated that the data can be influenced by the van der Waals-Casimir force due to the substrate. The current experiment was designed to measure not only the sticking probability of ultracold atomic hydrogen on bulk liquid ^{4}He but also the ^{4}He film thickness dependence of the sticking probability.

1.3 Overview of This Work

We measured the sticking probability of 300 μK to 4 mK atomic hydrogen on a superfluid ^{4}He film. The thickness of ^{4}He film on a sintered silver substrate varied from 0.5 nm to a bulk puddle. The results of this work reveal the onset of universal quantum reflection from the surface of bulk ^{4}He and also demonstrate the van der Waals-Casimir force due to the substrate as the film thickness is reduced.

The production and stabilization of ultracold atomic hydrogen is described in Chapter 2. Chapter 3 concerns the apparatus and the experimental techniques used in this work. The temperature, sticking probability, and the film thickness data are analyzed in Chapter 4. The results are presented and compared with the latest theories in Chapter 5 and the conclusions are summarized in the same chapter. In the final chapter, Chapter 6, design of a true quantum reflection experiment and a possible Casmir-Polder force study are discussed.

Chapter 2

Submillikelvin Atomic Hydrogen

Very cold hydrogen atoms are crucial for this surface reflection experiment. They are produced by trapping spin-polarized atomic hydrogen in a magnetic field. The trapped hydrogen is then evaporatively cooled to the desired temperatures. In this chapter I will briefly review magnetic trapping and evaporative cooling of spin-polarized hydrogen and describe the measurements of the energy distribution, temperature, total number and density of the trapped atoms.

2.1 Magnetic Trapping of Spin-Polarized Atomic Hydrogen

Atomic hydrogen is the simplest atom. When the electron spins are aligned, the weakly interacting atoms form the only substance which remains a gas at $T = 0$ [17, 18]. These qualities make spin-polarized hydrogen one of the best candidates for many fundamental experiments. However, hydrogen normally exists in the molecular state. Two hydrogen atoms recombine into molecular hydrogen, giving up 4.48 eV of recombination energy, when the electron spins are in the singlet state. This recombination process requires a third body in order to conserve both energy and momentum. The third body can be either another atom if the density of hydrogen atoms is high enough, or the wall of a container which confines atoms. On the other hand, two

16
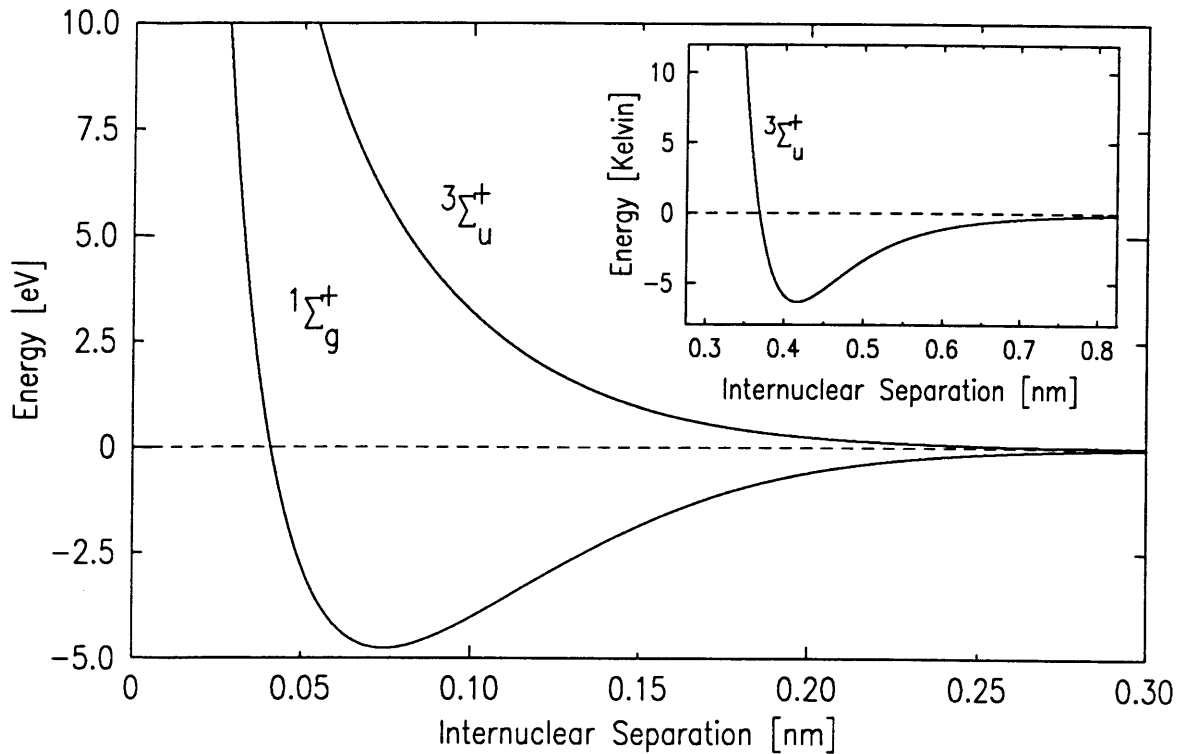
Figure 2-1: Interatomic potentials for two hydrogen atoms, calculated by Kolos and Wolniewicz [23].

hydrogen atoms can be stabilized against the formation of a molecule if the electron spins are in the triplet state. This is because the weak triplet potential supports no bound state as shown in Figure 2-1. However, the weak attractive minimum of the triplet potential at large separation is comparable to that of the potential between helium atoms. A detailed description of spin-polarized hydrogen and much of the early research can be found in the review articles of Greytak and Kleppner [19], and Silvera and Walraven [20]. Recent work on trapping and cooling is covered in the thesis of Doyle [21], and of Sandberg [22]. Only an outline of the preparation of cold hydrogen will be given here.

The hyperfine splitting of the ground state of atomic hydrogen in a magnetic field is shown in Figure 2-2. The four states are labeled $|a\rangle$, $|b\rangle$, $|c\rangle$ and $|d\rangle$ in order of

17
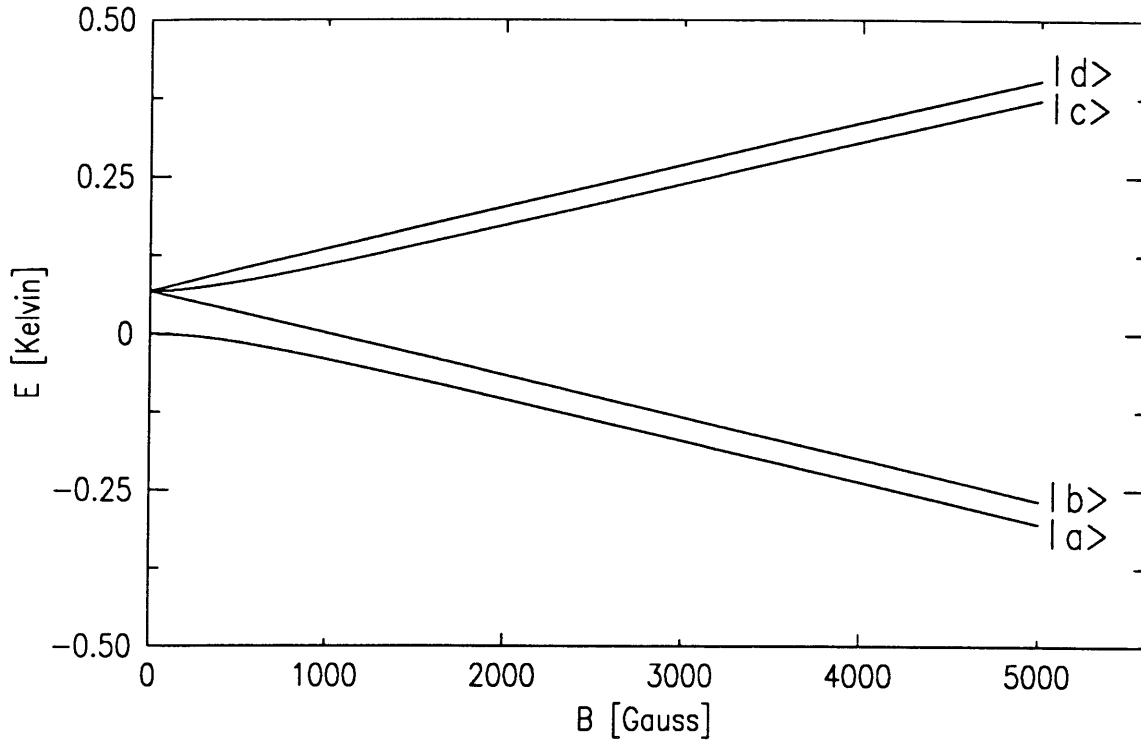
Figure 2-2: Hyperfine energy levels for ground state atomic hydrogen in a magnetic field.

increasing energy. Their expansions in proton and electron eigenstates are

$$|a\rangle = \cos\theta \, |\!\downarrow\uparrow\rangle - \sin\theta \, |\!\uparrow\downarrow\rangle$$

$$|b\rangle = |\!\downarrow\downarrow\rangle$$

$$|c\rangle = \cos\theta \, |\!\downarrow\uparrow\rangle + \sin\theta \, |\!\uparrow\downarrow\rangle$$

$$|d\rangle = |\!\uparrow\uparrow\rangle$$

where the first arrow indicates the electron spin state and second arrow indicates the proton spin state. θ is given by

$$\tan 2\theta = \frac{506}{B}$$

where B is the magnetic field in Gauss. It is clear from the above that $|b\rangle$ and $|d\rangle$

18

are pure electron spin states. Gases formed exclusively from one or the other these states will be stable against recombination. On the other hand, atoms in $|a\rangle$ (and $|c\rangle$) have some amount of the opposite spin and thus may recombine even with an atom in $|a\rangle$ or $|b\rangle$ (and $|c\rangle$ or $|d\rangle$). $|a\rangle$ and $|b\rangle$ atoms are called high-field seekers, because their energy is lower in high magnetic field. Similarly, $|c\rangle$ and $|d\rangle$ atoms are low-field seekers, because their energy is lower in low magnetic field. Consequently, a magnetic field minimum can attract and trap low-field seekers and a magnetic field maximum can attract and trap high-field seekers.

The surface density σ of atomic hydrogen on some surface is related to its bulk density n at equilibrium temperature T by

$$\sigma = n\,\lambda(T)\,e^{E_B/k_B T} \tag{2.1}$$

where $\lambda(T)$ is the thermal de Broglie wavelength and E_B is the binding energy of atomic hydrogen on the surface. The lowest possible values of E_B occur for liquid helium films ($E_B \approx 1$ K for ^{4}He and 0.4 K for ^{3}He). For any usable bulk density at 1 mK, the surface recombination associated with a saturated monolayer coverage makes the life time of the gas very short. It is obvious that a wall-free trap must be provided to cool spin-polarized hydrogen to the submillikelvin temperature regime. A static magnetic field maximum in free space is forbidden by Maxwell's equations. Trapping the high-field seekers in free space is not feasible. Hence, a cold spin-polarized hydrogen gas can only be realized by trapping the low-field seekers in a magnetic field minimum.

The magnetic trap that generates a field minimum in free space is constructed by two pinch solenoids, a quadrupole magnet and a bias solenoid as shown in Figure 2-3. The magnitude of the vector field in the trap has cylindrical symmetry and so does the potential energy due to the interaction between the magnetic moment of the hydrogen atom and the magnetic field, viz. $U(\vec{r}) = \mu_B B(\vec{r})$ where μ_B is Bohr magneton. The quadrupole magnet provides the field gradient in the radial direction and the pinch solenoids provide longitudinal confinement. The bias solenoid assures that the field

19
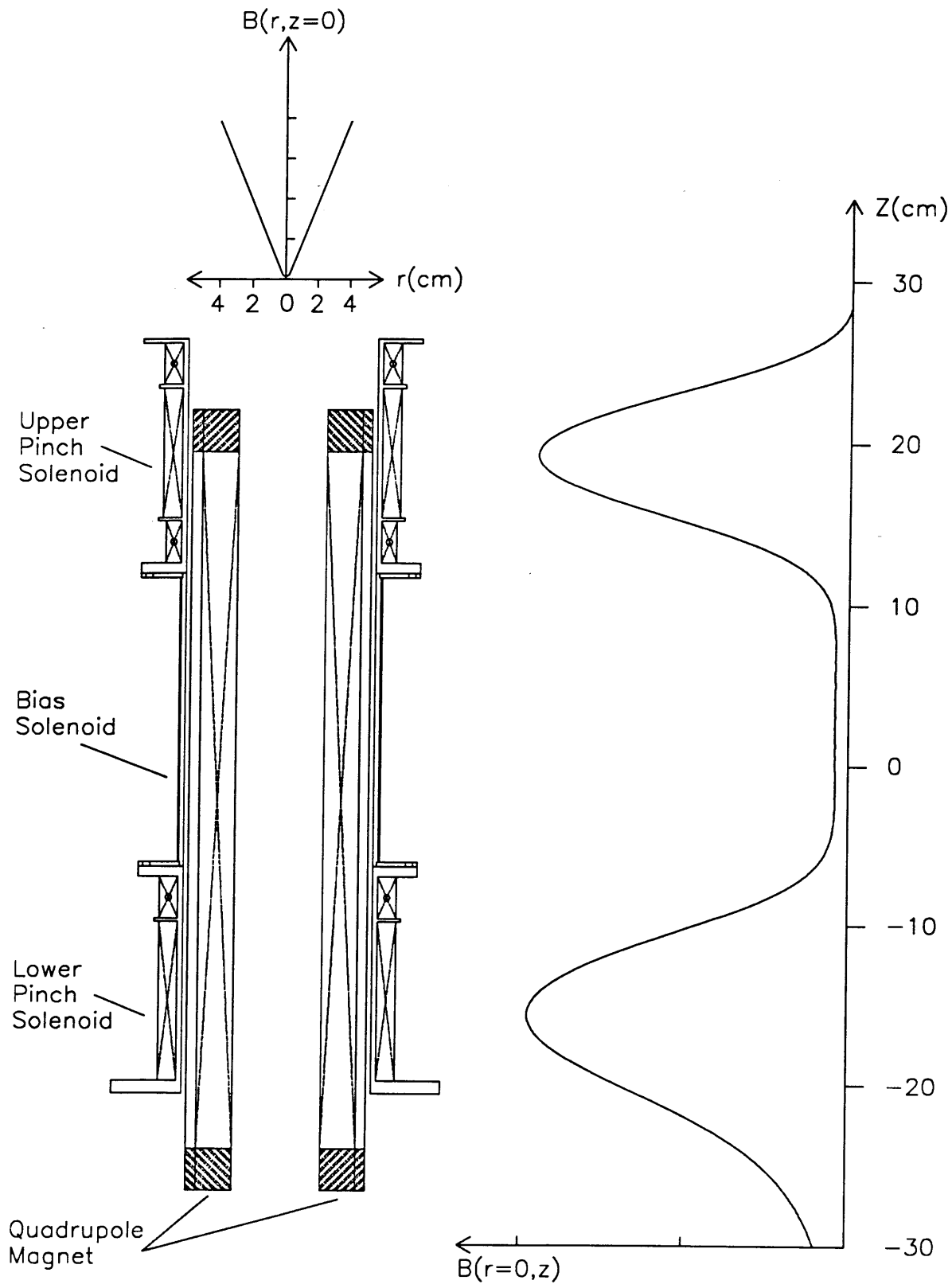
Figure 2-3: Trapping magnets and field profile.

in the trap region never vanishes, thereby preventing atoms from undergoing non-adiabatic spin-flip transitions.

Once the low-field seekers are in the trap, all $|c\rangle$ atoms will disappear quickly due to the dominant spin-exchange interaction [24], $|c\rangle + |c\rangle \rightarrow |b\rangle + |d\rangle$ [25, 26]. For our trap, the time scale for $|c\rangle$ atoms to vanish is a few seconds [27]. The resulting $|b\rangle$ atoms are ejected from the trap by the field gradient. Then only $|d\rangle$ atoms remain in the trap and doubly spin-polarized atomic hydrogen is established. The lifetime of $|d\rangle$ atoms is limited by dipolar electron-spin relaxation [24]. The dominant relaxation process is $|d\rangle + |d\rangle \rightarrow |a\rangle + |a\rangle$ [25, 26]. The decay time constant of this process for a typical condition of our experiment is about 200 seconds. This long life time enables us to do the experiment in a reasonable time scale. The method used to cool the gas further will be discussed in the next section.

2.2 Forced Evaporative Cooling

To carry out forced evaporative cooling the magnetic field intensity is slowly decreased so that the high energy atoms are removed from the trap. Then, the remaining atoms re-thermalize and the temperature of the trapped gas becomes colder. This is a very efficient cooling process. A one order of magnitude loss in atom number can cause a two order of magnitude drop in temperature [28].

A schematic version of the field profile for the magnetic trap in Figure 2-3 is shown in Figure 2-4. The trap depth, E_t, is determined by the energy difference between the trap barrier height and the bottom of the trap. Only atoms with energy below E_t can be confined in the trap and eventually approach a steady state of thermal equilibrium. In thermal equilibrium, the trapped atoms should be in a Maxwell-Boltzmann distribution truncated at E_t with a definite temperature, T, as shown in Figure 2-4. Measurement of the Maxwell-Boltzmann distribution of the trapped atoms will be discussed in the next section.

The steady state of the trap is actually a balance between a cooling mechanism and a heating mechanism. The heating mechanism is due to dipolar electron-spin

21
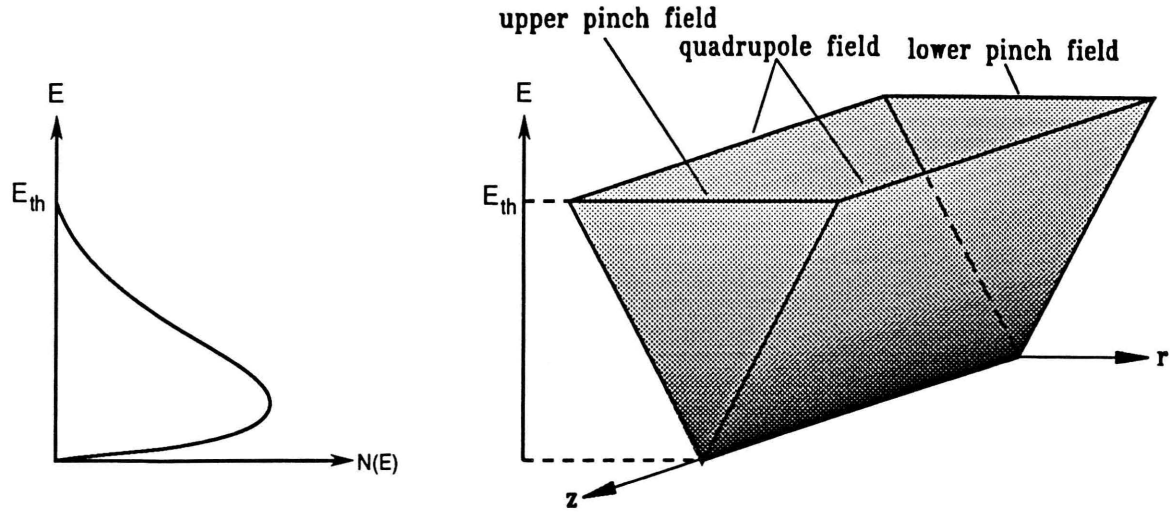
Figure 2-4:   Sketch of the magnetic trap (darker color indicates higher atom density) and truncated Maxwell-Boltzmann distribution.

relaxation, a two-body decay process. This decay process happens much more often in the high density region where the energy of the atoms is low. Consequently, the dipolar electron-spin relaxation removes atoms predominately with energy below the the average energy of the trap. This increases the average energy of the remaining trapped atoms. The cooling mechanism is due to evaporation from the trap. Some of the elastic collisions between the trapped atoms create atoms with energy above the threshold. These high energy atoms can no longer stay in the trap and each carries away an energy much greater than the average energy of the trap. The average energy of the trapped atoms is therefore reduced by this evaporation process. These two processes are illustrated in Figure 2-5. The dipolar relaxation rate depends primarily on the density. Because the density is higher for lower temperatures in a given trap, the dipolar relaxation rate increases with decreasing temperature. In contrast, the evaporation rate has positive temperature dependence, because a higher temperature brings the atoms closes to the threshold energy. The balance of these heating and cooling rates determines the temperature of the trapped atoms in terms
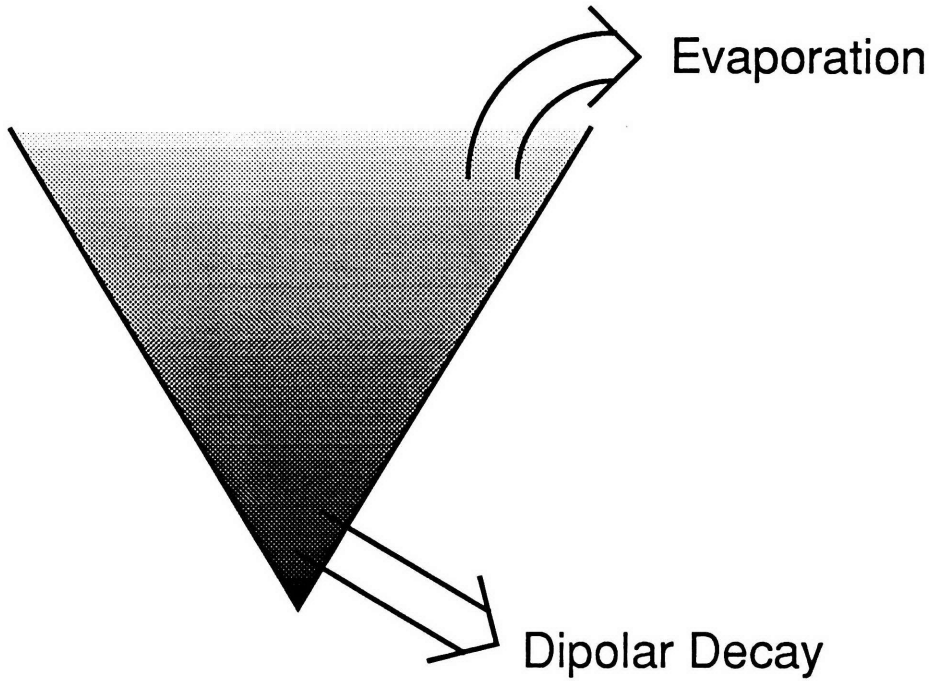
Figure 2-5: Decay processes in a trap.

of the threshold energy as

$$k_B T = \frac{E_t}{\eta} \qquad (2.2)$$

where η is normally around 10 for our trap [28]. Therefore, one can cool the gas in the trap to the desired temperature by bringing down the trap depth slowly, i.e. by preserving Equation 2.2 during the course. The time to perform this process is usually about 5 minutes. This technique is called forced evaporative cooling and was first proposed by Hess [29].

Density is another important property of the trapped atoms. It is determined by the ratio of the quadrupole field to the pinch fields at the end of forced evaporative cooling as illustrated in Figure 2-6. When the quadrupole field is kept constant, the trap has a small volume after forced evaporative cooling. On the other hand, if the quadrupole field to pinch fields is kept constant, the trap will have a larger volume after forced evaporative cooling. For the same number of atoms in a given trap depth,
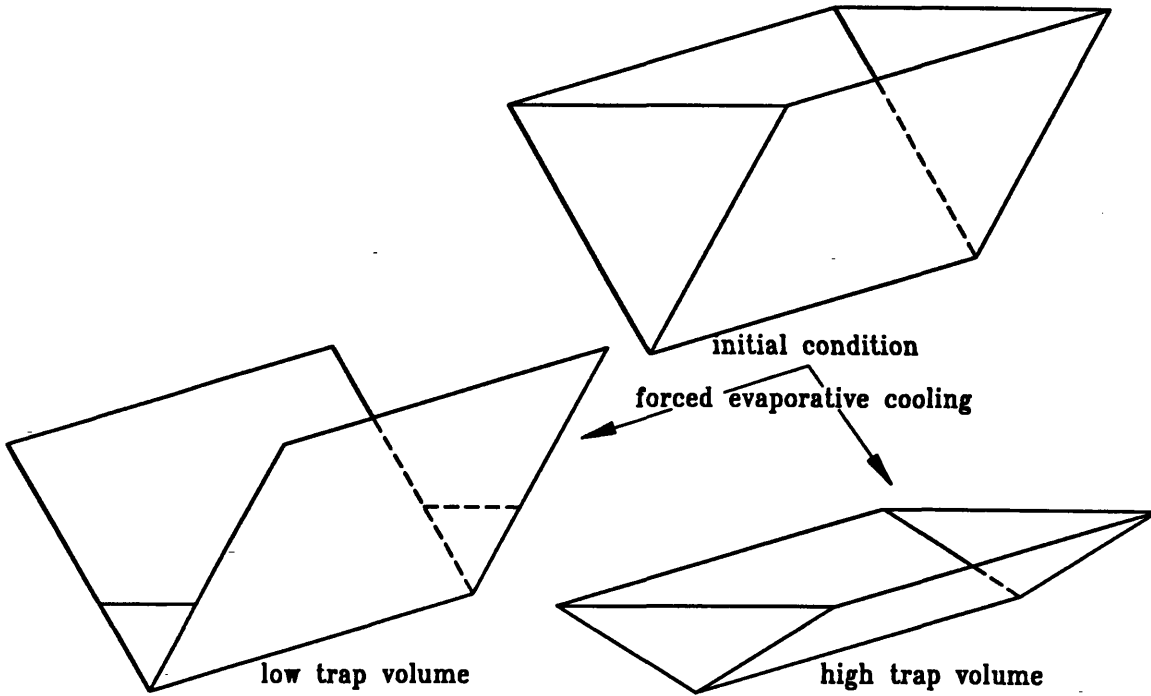
Figure 2-6: Compression of trap volumes for different cooling paths.

the density is much higher in the small trap volume than in the larger trap volume. For this reason, a desired density can be achieved by varying the ratio of the two fields at the end of forced evaporative cooling.

To summarize, forced evaporative cooling decreases the temperature of the trapped atoms to one tenth of the trap depth, at the expense of atom number. Setting the ratio of the quadrupole field to pinch fields adjusts the density of the atoms in the trap. Both temperature and density can be independently varied according to desired experimental conditions.

2.3 Macroscopic Quantity Measurement of Trapped Atoms

Once trapped atoms achieve the desired experimental conditions, one can measure their temperature, number, and density by employing a bolometric technique. The

basic idea of the technique is to lower E_t to zero linearly in time and detect the atom flux coming out of the trap. (The flux measurement will be described in Section 3.3.) By recording E_t and the atom flux simultaneously in time, an energy distribution of the trapped atoms is obtained (illustrated in Figure 2-7). The detection time for lowering E_t to zero is about 10 sec. This detection time is much shorter that the equilibrium time, about 100 sec, of the trapped atoms. Therefore, the measured energy distribution represents the conditions in the trap before detection.

The temperature of the trapped atoms is determined by fitting the measured energy distribution to a calculated energy distribution function based on Maxwell-Boltzmann statistics. The calculated energy distribution function, $n(E)$, is given by

$$n(E) \propto \frac{d}{dE} \int\int_{0 \leq H(\vec{r},\vec{p}) \leq E} e^{-H(\vec{r},\vec{p})/k_B T} \, d^3\vec{p}\, d^3\vec{r} \qquad (2.3)$$

where $H(\vec{r},\vec{p}) = U(\vec{r}) + \vec{p}^2/2m$ and $U(\vec{r})$ is the potential energy in the trap for both magnetic field and gravity. The temperature and the amplitude of the calculated energy distribution function are the adjustable parameters in the fitting. For an ideal trap as in Figure 2-7, the above equation leads to

$$n(E) \propto (E/k_B T)^{2.5} \, e^{-E/k_B T}. \qquad (2.4)$$

The field profile of this ideal trap is described by

$$B(r,z) = \begin{cases} kr & \text{for } 0 < z < L \\ E_t/\mu_B & \text{for } z = 0 \text{ and } z = L \\ 0 & \text{otherwise} \end{cases} \qquad (2.5)$$

where k is a field gradient constant, L is the trap length, and μ_B is Bohr magneton. The magnetic field profile of our trap is determined through numerical integration over the currents of all the magnets with the Biot-Savart law. The uncertainty of the magnetic field obtained from the numerical integration is the larger one among 1%
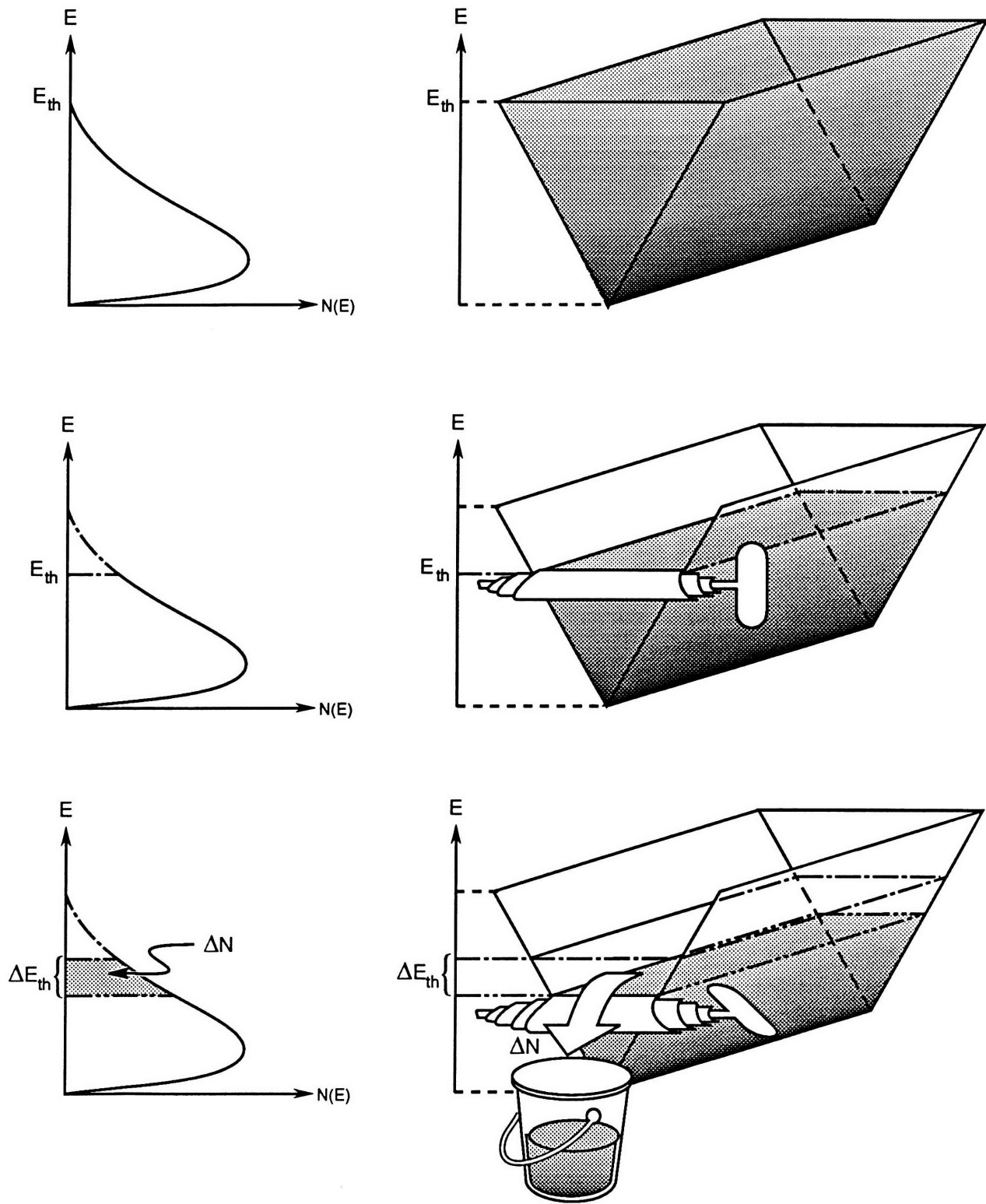
Figure 2-7: Energy distribution measurement.
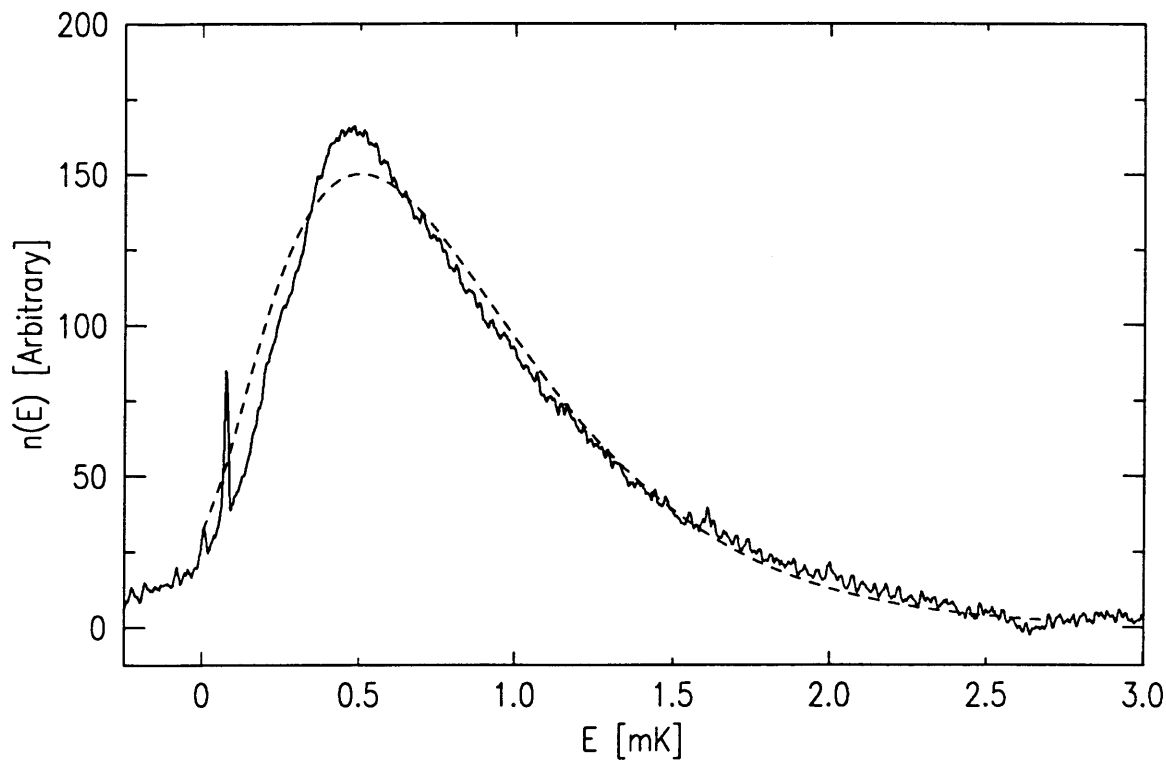
Figure 2-8:   Energy distribution of the trapped atoms. The solid curve is measured energy distribution for $E_t = 2.7$ mK. The dashed curve is calculated energy distribution functions according to Equation 2.3 with the actual field profile of our trap and $T = 300 \ \mu$K.

of the field and 1 Gauss. This uncertainty is verified by comparing the field obtained from the integration with the measured field. The field profile of our trap is close to the one of the above ideal trap. An example of the temperature determination is given in Figure 2-8. The temperature determination will be discussed more throughout in Section 4.1.

The area below the energy distribution curve, N_s, is proportional to the atom number, N,

$$N = pN_s. \tag{2.6}$$

In order to determine atom numbers, the constant of proportionality, p, is calibrated using dipolar electron-spin relaxation. This decay is the dominant atom loss mecha-

nism when the trap is kept static. The equation for the decay is

$$\frac{\partial\, n(\vec{r})}{\partial t} = -g\, n(\vec{r})^2 \tag{2.7}$$

where $n(\vec{r})$ is the density and g is the dipolar electron-spin relaxation constant. Usually g is temperature- and field-dependent, but in our low temperature regime and for the trapping fields of this experiment g can be assumed to take its value at $T = 0$ and $B = 0$, viz. $g = 10^{-15} \text{cm}^{-3}$ [25, 26]. After integrating both sides of the Equation 2.7 over the trap volume, we have

$$\frac{dN}{dt} = -g\alpha N^2 \tag{2.8}$$

where

$$\alpha = \frac{\int n(\vec{r})^2\, d^3\vec{r}}{(\int n(\vec{r})\, d^3\vec{r})^2} \quad . \tag{2.9}$$

α is only temperature and field profile dependent and can be calculated without knowing the absolute atom number. Equation 2.6 and Equation 2.8 lead to

$$\frac{dN_s^{-1}}{dt} = g\alpha p \quad . \tag{2.10}$$

This implies the reciprocal of atom number in the trap is linearly dependent on time. By measuring the energy distributions after the loaded trap has been held for different periods of time following forced evaporative cooling, a plot of N_s versus time can be made (see Figure 2-9). The slope of the fitted line in Figure 2-9 is the product of g, α, and p. Since g and α are known, p is calibrated. A percent uncertainty in p of 5% comes from the fitting uncertainty in plots like Figure 2-9. The uncertainty of p contributed from α is mainly due to the uncertainty of the atom temperature. As long as p is calibrated, the atom number in the trap at any time can be evaluated from the area below the energy distribution curve.

Knowing the atom number and the temperature, one can calculate the density in
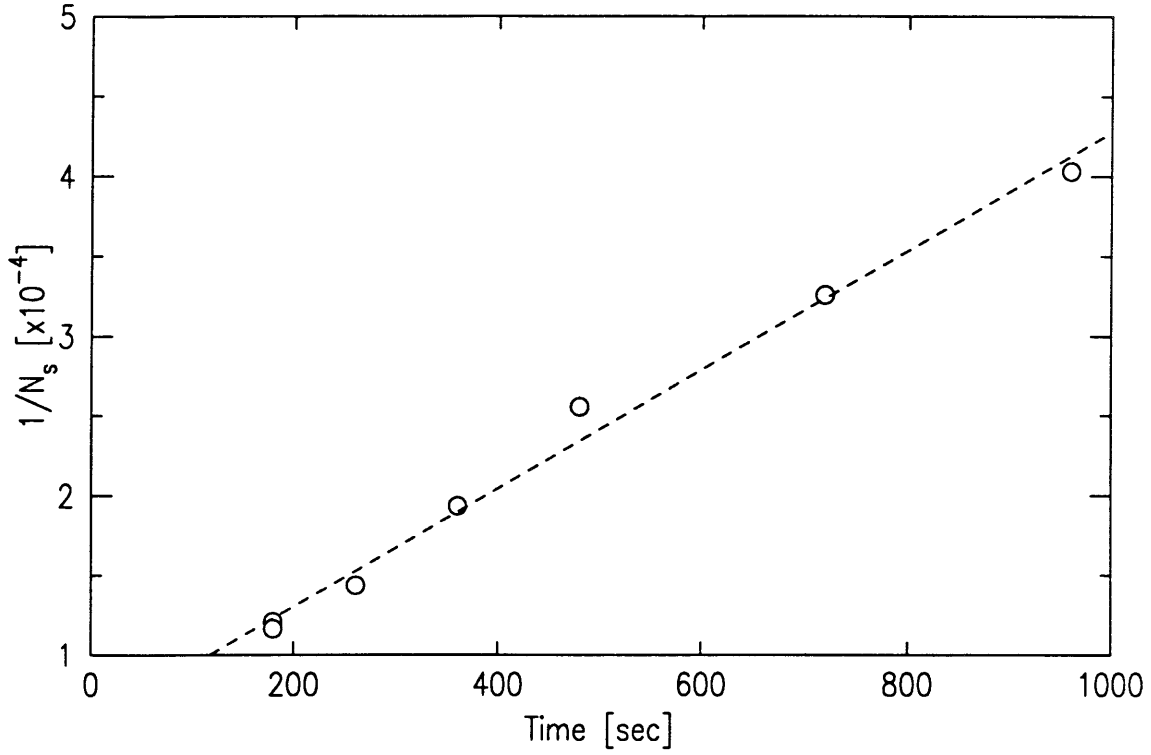
Figure 2-9: Dipolar electron-spin relaxation decay: reciprocal of total number of atoms remaining in a 2.7-mK-deep trap versus time. The slope of the dashed line calibrates the bolometer's signals.

the trap from the following equation:

$$n(\vec{r}) = \frac{N \int e^{-H(\vec{r},\vec{p})/k_B T} d^3\vec{p}}{\iint e^{-H(\vec{r},\vec{p})/k_B T} d^3\vec{p}\, d^3\vec{r}} \ . \tag{2.11}$$

The integration constraint is $0 \leq H(\vec{r},\vec{p}) \leq E_t$. Once the density and the temperature have been obtained, other macroscopic quantities can be deduced accordingly.

29

Chapter 3

Apparatus and Experimental Techniques

This chapter describes the apparatus and the experimental techniques developed for producing ultra cold hydrogen atoms and studying the collisions between the atoms and the liquid surface of superfluid ^{4}He. The cell, a cylindrical container, centered around the trapped hydrogen atoms, was coated with superfluid ^{4}He film in its inner wall. The cell was surrounded by a magnet system which generated the magnetic fields necessary to trap and manipulate the hydrogen atoms. A graphite film deposited on a quartz plate severed not only as a bolometer to measure the atom flux coming out of the trap but also as a film burner to measure the thickness of superfluid ^{4}He film. A sintered silver surface positioned at the very bottom of the cell served as a substrate for the superfluid ^{4}He film. The film thickness varied from 0.5 nm to 1 mm. Trapped atoms with temperatures ranging from 300 μK to 4 mK were brought into contact with the surface in order to measure the sticking probability. The arrangement of the apparatus is shown in Figure 3-1.
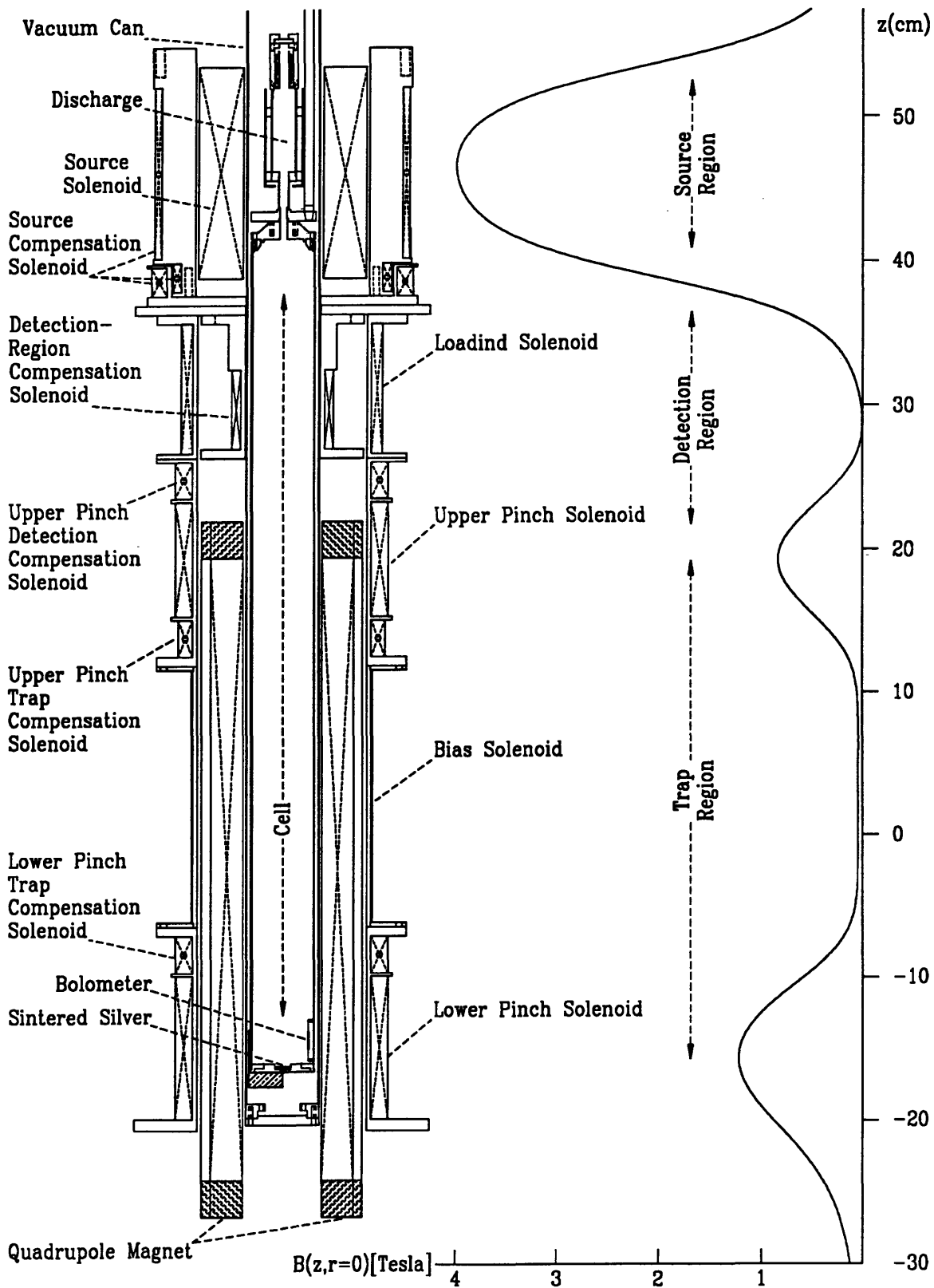
Figure 3-1: Scale drawing of the apparatus. The magnetic field profile corresponds to the initial condition of the forced evaporative cooling.

G-10 tube with
1$\frac{21}{32}$" I.D. and 1$\frac{23}{32}$" O.D.

160 25-gauge copper wires
run the length of the cell

layer of epoxy

cell is wrapped in Kevlar
and covered with 1266 epoxy
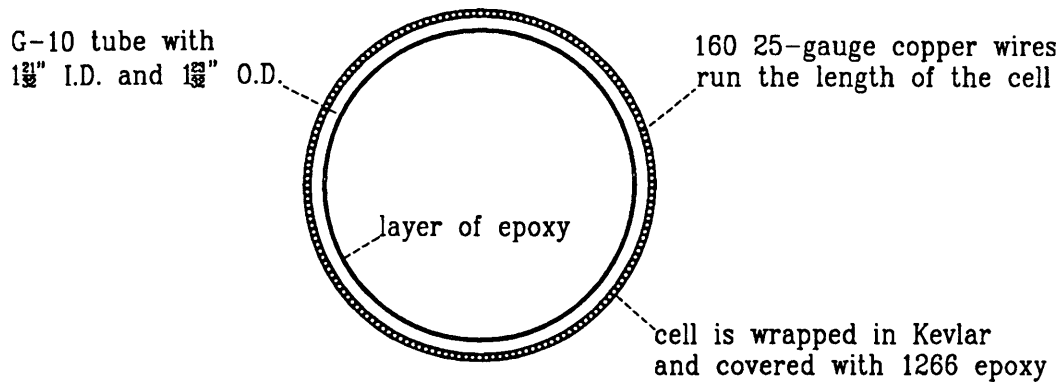
Figure 3-2: Top view of the cell. The epoxy inside the cell is the same as that used in Reference [21].

3.1 Cell

The cell is a cylindrical container 57 cm in length, with 2.1 cm inner radius and 0.15 cm wall thickness. It was mounted vertically in a ^{3}He-^{4}He Dilution Refrigerator System, Oxford Instruments Model 2000. The top flange of the cell was connected to the bottom of a discharge assembly where molecule hydrogen is dissociated The flange is thermally anchored to the mixing chamber of the refrigerator which can maintain the temperature of the cell below 70 mK. The cell wall is a metal, fiberglass, and epoxy composite (see Figure 3-2). It has metal-like high thermal conductance along the length of the cell but insulator-like low conductivity for circumferential eddy current heating. The high thermal conductance along the length of the cell can carry away any heat due to either hydrogen recombination or magnetic field ramping. In addition, the low eddy current heating of the cell wall reduces the temperature rise during magnetic field changes. The construction of the cell is similar to the one described by Reference [21]. Modifications of the construction made in order to perform this experiment will be discussed next.

A cell centering collar was made containing six Vespel spikes equally spaced around the circumference. See Figure 3-3. Vespel is an outstanding thermal insulator and has excellent machinability [30]. The spikes prevent the cell from touching the surround-
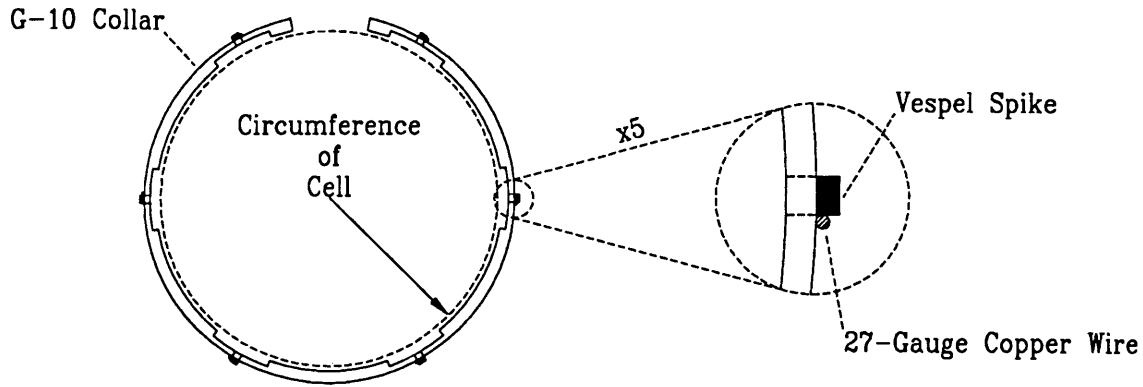
Figure 3-3:   Cell centering collar.

ing vacuum can, which was immersed in a liquid ^{4}He bath (4.2 Kelvin). Each spike is 0.6 mm long and 1 mm in diameter. The diameter of the spike is optimized for mechanical strength and thermal insulation. The end of the each spike is embedded in the G-10 collar, which hangs loosely around the cell. A copper wire is glued to the collar near each spike and thermally anchored at 0.3 Kelvin at the other end. The heat leakage through the cell centering collar is tolerable for the experiment and does not rise the temperature of the top flange of the cell higher than 50 mK under normal dilution refrigerator operation.

The bottom of the cell is illustrated in Figure 3-4. A 0.55 cm radius depression is made at the cell bottom for confining sintered silver. There is an oxygen free copper substrate underneath the silver sinter. The substrate is fabricated in the shape as shown in the inset of Figure 3-4 to minimize eddy current heating and plated with 300 nm of solid silver on its top surface. A 0.5 mm thick high purity copper foil [31] (hanging vertically) is attached to the bottom of the substrate on its one end and attached to the outer wall of the cell on the other end. This copper foil provides thermal anchoring for the substrate. A thick film Ru_2O chip resistor [32] is bonded to the foil and monitors the temperature of the substrate.

The sinter in the depression of the cell bottom is made from silver powder of 70 nm nominal particle size [33]. The powder was pre-heated at 50 °C in hydrogen

33

Top View of Copper Substrate

160 25-Gauge Copper Wires
Equally Spaced around Cell

Cell Wall

Bolometer

Cell Bottom Plate

Sintered Silver

Copper Substrate

Copper Foil

Chip Resistor Thermometer

G-10

oxygen free copper

silver

99.9985% purity copper

1 cm
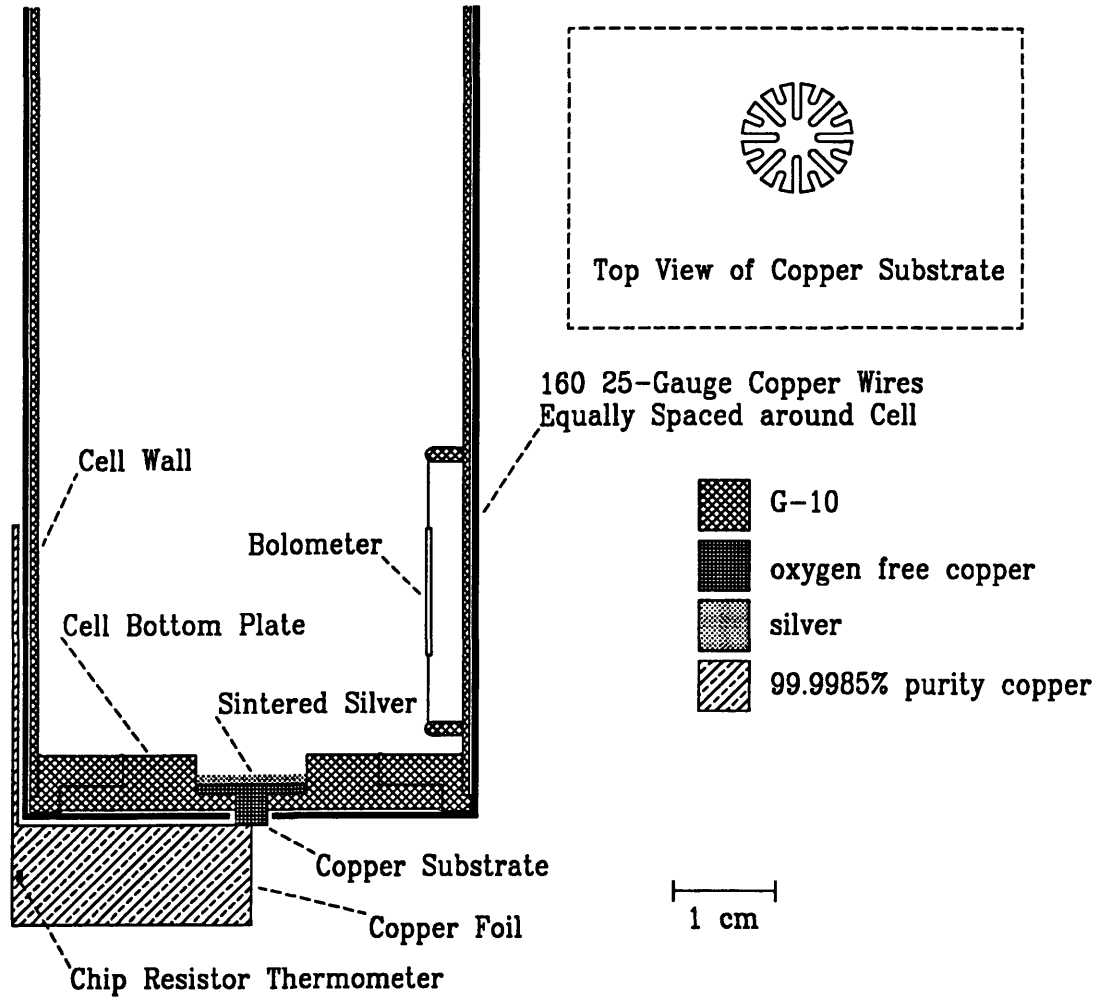
Figure 3-4: Blow up of cell bottom.

atmosphere for one hour and then pressed against the substrate in the depression
with 75×10^6 N/m^2 pressure. The 1-mm-thick packed powder was again heated at
100 °C in hydrogen atmosphere for half hour. Under these processes, the finished
sinter has about 1 m^2 surface area and 100 nm pore size by estimation [34, 35]. This
large surface area diminishes the Kapitza thermal resistance and assures thermal
equilibrium between the substrate underneath the silver sinter and the helium on the
top of the silver sinter. For the case that 10^{13} hydrogen recombinations per second
occur on the helium surface, the estimated temperature gradient between the 80-mK
copper substrate and the heated helium surface does not exceed 20 mK with the
assumption that effective surface area of the sinter is only 300 cm^2.

34

3.2 Experimental Sequence and the Field Profile of the Magnet System

Besides the quadrupole magnet, the upper pinch solenoid, the lower pinch solenoid, and the bias solenoid described in Section 2.1, the loading solenoid and source solenoid are also a part of the magnet system. The field profile generated by the magnet system can be broken into source, detection, and trap regions as shown in Figure 3-1. The magnet system and its corresponding magnetic field profile for a typical experimental sequence will be presented in this section.

The source solenoid provides the field in the source region which is always kept at 4 Tesla. A discharge located in the source region converts molecular hydrogen into atomic hydrogen. The high magnetic field expels $|c\rangle$ and $|d\rangle$ atoms and pulls back $|a\rangle$ and $|b\rangle$ atoms. While the discharge is being fired, the two pinch solenoids generated 1 Tesla (0.675 K) field barriers at the end of the trapping region. In addition, the quadrupole magnet generates a linear radial field gradient in the trap region with the magnitude of 1 Tesla (0.675 K) at the cell wall. An 1-Tesla magnetic field generated by the loading solenoid bridged between source region and trap region. The field profile during loading the trap is shown in Figure 3-5 (a). The hot atomic hydrogen coming from the source region dissipates its energy via thermalization with superfluid ^{4}He covered the cell wall. Some of those atoms lose energy by H-H and H-^{4}He collisions and become trapped.

After the trap is loaded and the discharge turned off, the loading solenoid is brought to zero. Consequently, a detection region is established between the source region and the trap region. There is no radial field confinement in the detection region and any atoms in the detection region can access the cell wall. Forced evaporative cooling starts right after the detection region is established. The field intensities generated by the pinch solenoids and quadrupole magnet are decreased slowly such that the trapped atoms are cooled to the desired temperatures and densities for the experiment. The bias solenoid is always kept constant during the forced evaporative cooling. The field profile changes from the one in Figure 3-5 (b) to (c). At the end

of the forced evaporative cooling, the trapped atoms form a cylindrical gas cloud 0.5 mm in radius and 18 cm in length. The lower end of the gas cloud is 7 cm above the cell bottom. The temperature of the gas varies from 300 μK to 4 mK and the gas density on the axis is typically 10^{13} cm^{-3}.

During the forced evaporative cooling, the bottom of the cell is shielded by the field generated by the lower pinch solenoid. Thus, the trapped atoms can never reach the sintered silver surface covered by the superfluid ^{4}He at the bottom of the cell.
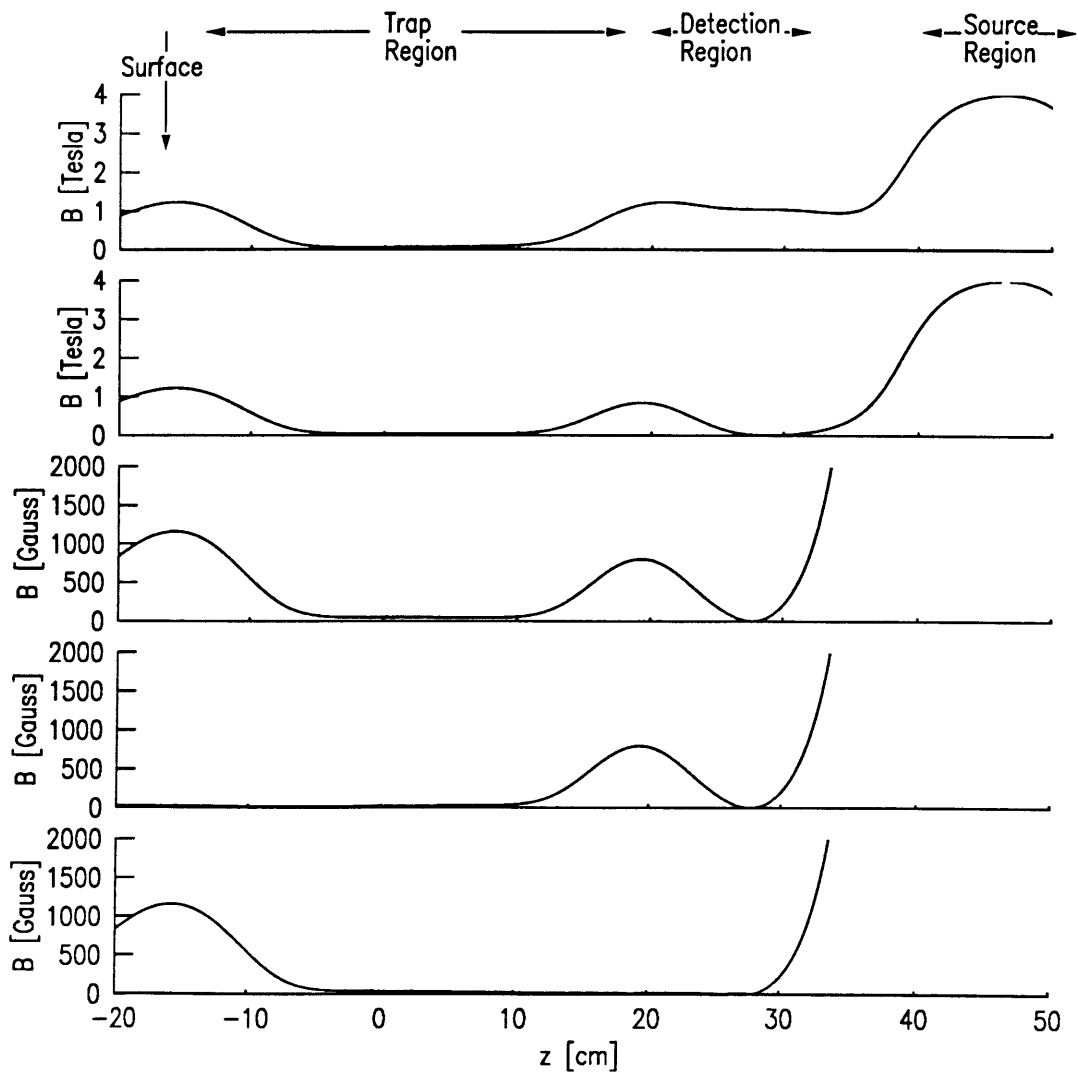
Figure 3-5: Magnetic field profiles on the axis of a typical experimental sequence. (a) Loading trap. (b) Beginning of forced evaporative cooling. (c) End of forced evaporative cooling. (d) Surface collision. (e) Dumping atoms.
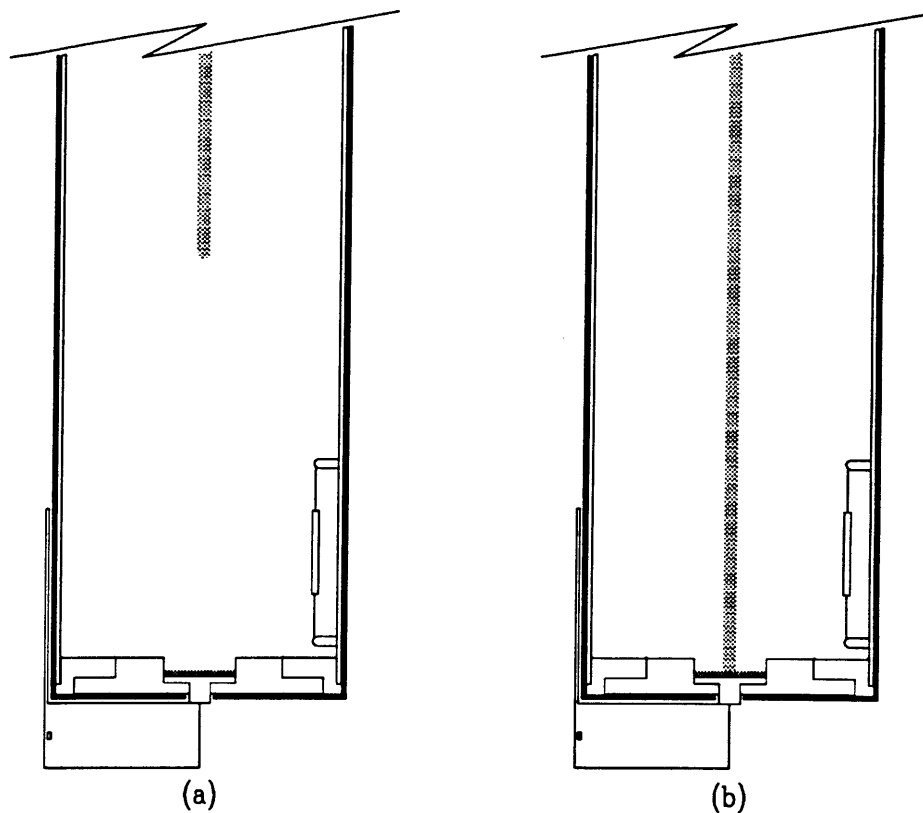
Figure 3-6: Schematic diagram of atoms brought into contact with the helium surface. The shaded region indicates atom cloud. (a) The lower pinch solenoid is on. (b) The lower pinch solenoid is off.

When sticking probability measurements are performed, the lower pinch solenoid is turned off instantaneously (see Figure 3-5 (d)). The trapped atoms can now contact the surface at the cell bottom as illustrated in Figure 3-6. Atom-surface collisions are restricted to the area within the depression due to the radial compression by the quadrupole field . After the surface was exposed to the trapped atoms for a certain contact interval, the lower pinch field was brought back to the same intensity as the one before the lower pinch solenoid was switched off. The atoms remaining in the trap at the end of the contact interval were the ones surviving from the surface collisions.

In order to measure the parameters of the trapped atoms before or after the contact intervals the atoms must be dumped to the detection region by ramping down the upper pinch field to zero linearly. This is shown in Figure 3-5 (e). The designed detector of the atom flux is a bolometer located at the detection region.

This bolometer was out of order during the course of the experiment. Therefore, the atom flux coming out of the trap was measured by a bolometer located near the bottom of the cell. The bolometric detection technique will be discussed in the next section.

The field profiles and the experimental sequence presented above are for a single measurement. The time to carry out such an experimental sequence is about 5 minutes. Sticking probability measurements, temperature determinations, density evaluations, and any other experiment related verifications were obtained by performing a number of related experimental sequences.

3.3   Bolometer and Measurement of Atom Flux

A bolometer is located on the inner wall of the cell 1.8 cm above the sintered silver surface. The design of the bolometer shown in Figure 3-7 is based on the one described in Reference [21]. The constructing procedure is summarized here. A fine polished X-cut single crystal quartz plate of $0.5\times0.5\times0.001$ inch^3 formed the base of the bolometer. Two electrodes were created on the quartz plate by thermally evaporating two strips of 100 Å thick chromium and then 1000 Å thick gold. The gap between the electrodes was about 0.015 inch. After the electrodes were made, four nylon fibers of 0.0035 inch diameter were glued to the four corners of the quartz plate with GE varnish used to suspended the quartz plate from its G-10 mount. A 34 μm diameter NbTi superconducting coil was bonded to each electrode of the suspended quartz plate with bonding agents of silver paint and Stycast 1266 epoxy [36]. Finally a graphite film, Aerodag [37], was deposited on the gap between the electrodes little by little until the resistance across the gap was below 1 kΩ. The resulting bolometer has low heat capacity, good thermal conductivity between resistive area and the rest of the bolometer, weak thermal coupling to the environment, and a sensitive temperature dependence of the resistance.

The bolometer functioned as a temperature transducer. It was heated and maintained at 300 mK by employing a constant temperature circuit [38], which applied
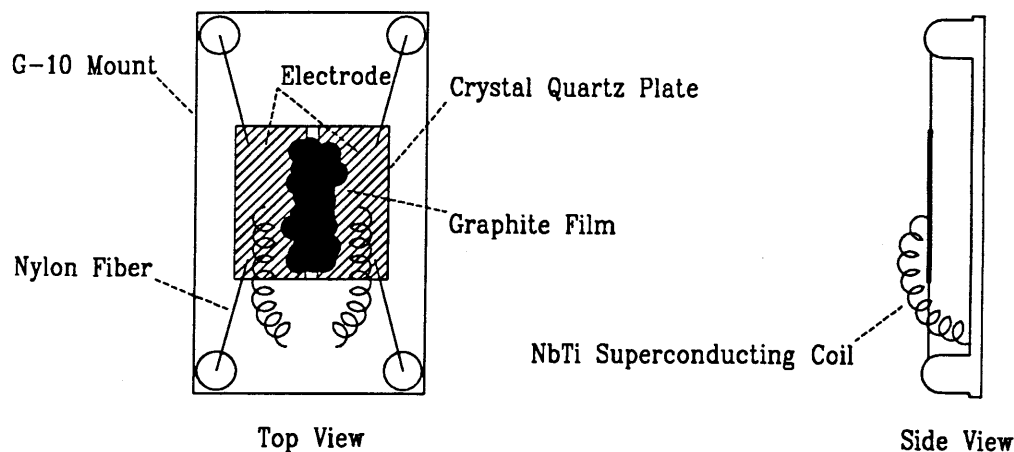
Figure 3-7: Structure of the bolometer.

bias resistive heating of 6 nW. Any other heating on the bolometer decreases this bias resistive heating. The sensitivity and the bandwidth of the heating detection of the bolometer are about 1 pW and 100 Hz respectively. This 1 pW sensitivity is equivalent to the total heat released by 10^6 hydrogen recombinations per second.

The bolometric detection was used in this experiment to measure the atom flux coming out of the trap. When the trapped $|d\rangle$ atoms were dumped to the detection region by lowering the upper pinch field to zero as described in the previous section, they bounced around in this region. Because there was no radial field confinement in the detection region, any atom bouncing around this region eventually stuck to the cell wall which was covered by sub-saturated or saturated superfluid ^{4}He film. The ^{4}He film on the wall was always very thin in the detection region due to the height, approximately 45 cm, of the detection region above the cell bottom. The saturation ^{4}He film thickness at this height is much less than 1 nm. The sticking probability at the detection region was kept high, according to the thickness dependence of the sticking probability reported in Chapter 5. Therefore, this high sticking probability assured that the atom stuck to the cell wall quickly. Once a $|d\rangle$ atom stuck to the wall, it first spin relaxed to a high field seeking state due to small magnetic impurities on the surface of the wall then recombined with another incoming $|d\rangle$ atom to form a molecule. The resulting molecules bounced around the cell and

deposited the recombination energy to the wall or the bolometer. It has been verified that the signal of the bolometer due to the recombination heating is linear to the atom flux coming out of the trap under normal operation. The verification was performed through the comparison of bolometer signals resulted from varied atom flux at the same trapping condition. The atom flux was varied by adjusting the rates of zeroing the upper pinch field. The calibration of the bolometer signal is described in Section 2.3, but the calibration is not necessary in this experiment. Moreover, hydrogen molecule loses about 90 percent of its recombination energy in 10 bounces with the sub-saturated superfluid ^{4}He covered surface. This result is deduced from the comparison between the bolometer signal of dumping atoms into the detection region and that of dumping atoms into the bottom of the cell, while superfluid ^{4}He is sub-saturated in the cell. In conclusion, the bolometric technique described here is suitable for detecting the atom flux coming out of the trap within the experimental precision.

3.4 Film Burner and Measurement of Film Thickness

The bolometer described in the previous section also served as a helium film burner, which measured the film thickness of superfluid ^{4}He . The measurement method is to apply a constant current to resistively heat the film burner. A part of the applied heat power evaporates the ^{4}He film from the surface of the film burner. While this is happening, the resistance (and therefore the temperature) of the film remains constant as shown in Figure 3-8. The rest of the applied heat flows away from the bolometer, by helium film flow and conduction along the leads, at a rate P Watt. P depends only on the temperature difference between the bolometer and the cell wall; thus, it is a constant while the film is evaporating. However, when all the ^{4}He film on the surface of the film burner has been removed, the temperature of the film burner suddenly rises to a higher value. The resistance and the voltage across the film burner
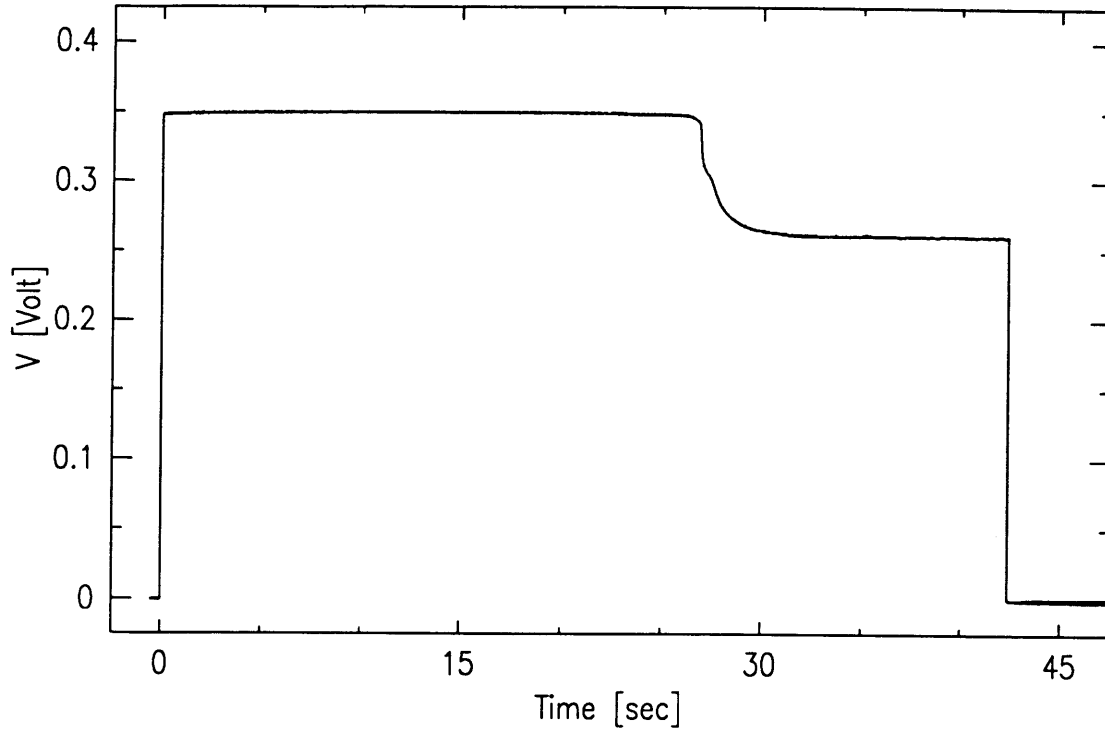
Figure 3-8:   Voltage across film burner covered by 10 nm thick ^{4}He film during application of heating. The supplied current is 80 μA. The kink of the voltage curve indicates $t_b = 26.6$ sec.

then decrease abruptly as shown in Figure 3-8. By measuring the voltage across the film burner, the time interval, t_b, before the abrupt decrease of the voltage, and the current through the film burner, one can calculate the total energy, $E(t_b)$, applied to the film burner before the film disappears. By adjusting the applied current through the film burner, t_b and $E(t_b)$ are varied and the following energy balance equation can be mapped out:

$$E(t_b) = E_0 + P\,t_b \qquad (3.1)$$

where E_0 is the burning energy required to evaporate all the ^{4}He film from the surface of the burner. Typical $E(t_b)$ versus t_b data are shown in Figure 3-9. The intersection between the fitted line and $E(t_b)$ axis in the figure indicates E_0.

The burning energy, E_0, depends linearly on the thickness of the film on the
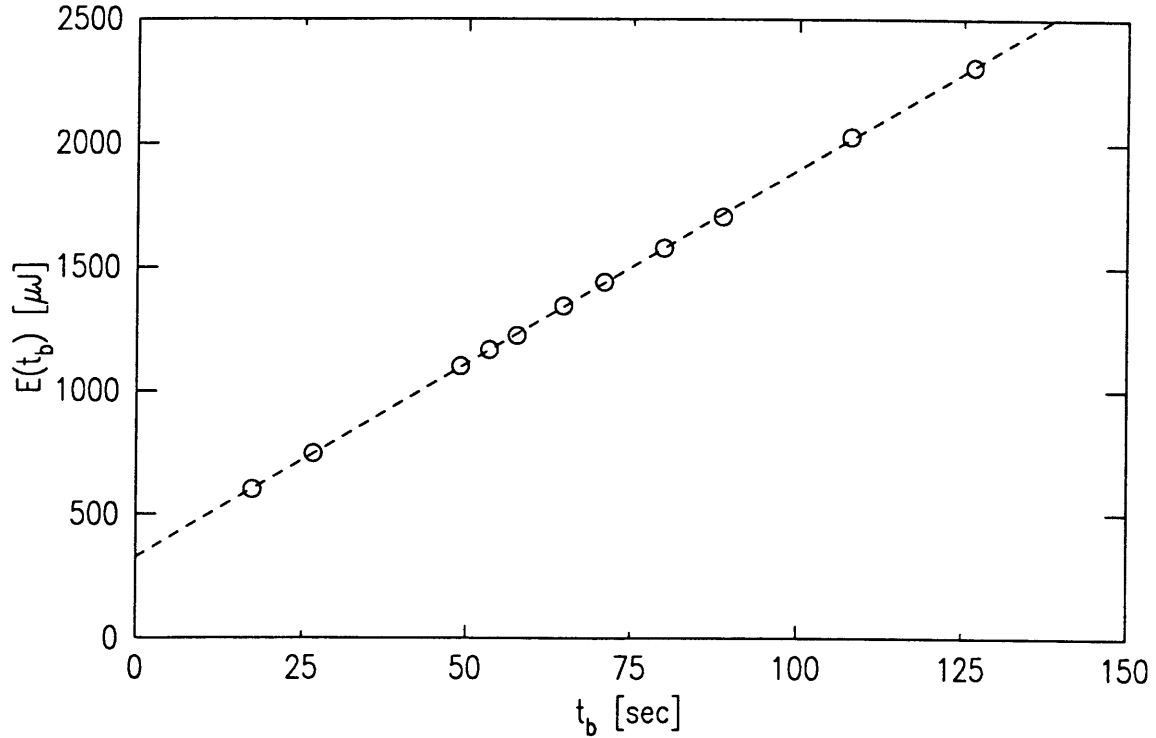
Figure 3-9: Typical data of total applied energy versus time interval of film burning. The dashed line indicates $E_0 = 330$ μJ, corresponding a 10 nm thick ^{4}He film.

surface of the burner. Based on the height of the film burner above the lowest point of the cell, the saturated film thickness at the film burner is 24 nm [39]. This value calibrates the film thickness measurements at sub-saturated film coverages, as will be shown in Section 4.4. Because of the superfluidity of ^{4}He we make the assumption that the thickness of the sub-saturated ^{4}He film on the burner is the same as that on the top of the sintered silver surface.

3.5 Sticking Probability Measurement

When sticking probability measurements are performed. the trapped $|d\rangle$ atoms with a temperature ranging from 300 μK to 4 mK are brought into contact with the surface at the bottom of the cell. This contact is achieved by turning off the lower pinch

solenoid as shown in Figure 3-5 (d) and Figure 3-6. The atom-surface collisions are restricted to the circular area of 0.5 mm radius on the superfluid ^{4}He film covering the sintered silver surface. The thickness of the ^{4}He film on the surface varied from 0.5 nm to 1 mm. After the surface is exposed to the atoms for a certain contact interval, t_c, the lower pinch field is switched back to the original intensity. The transient time of turning on or off the lower pinch solenoid varied from 0.1 s to 1 s. This transient time was chosen as short as possible so that the heating due to ramping the field didn't disturb the measurement. After being held in the trap for some time interval after the lower pinch field was restored, the remaining atoms are dumped into the detection region and measured by the bolometer. For a single data point of the sticking probability, the above procedure was carried out for a number of t_c's at the same atom temperature, ^{4}He film thickness, and other experimental conditions.

During the contact interval, the $|d\rangle$ atoms travel in the volume defined by the surface, the upper pinch field barrier, and the quadrupole field. An atom can either stick to or reflect from the surface during an atom-surface collision. Once a $|d\rangle$ atom stuck to the surface, it spin relaxes to a high field seeking state due to small magnetic impurities on the surface and permanently disappears from the trap. Therefore, the number of atoms remaining in the trap after the contact decays with t_c. Figure 3-10 shows the bolometer signals upon dumping the remaining atoms into the detection region for various t_c's. The area of the signal, N_s, indicates the number of remaining atoms and is reproducible to better than 10% for the repeated measurements. The N_s is plotted against t_c in the inset of Figure 3-10. The decay rate, τ_s^{-1}, due to sticking to the surface can be evaluated by fitting the data points in the inset with a function describing the decay (see the dashed curve in the inset). Knowing the atom-surface collision rate, τ_c^{-1}, one can measure the sticking probability, $s(T)$, at an atom temperature, T, and a given ^{4}He film thickness according to the equation,

$$s(T) = \tau_s^{-1}/\tau_c^{-1} \ .$$

(3.2)

The sticking probability is expected to be independent of surface temperature as
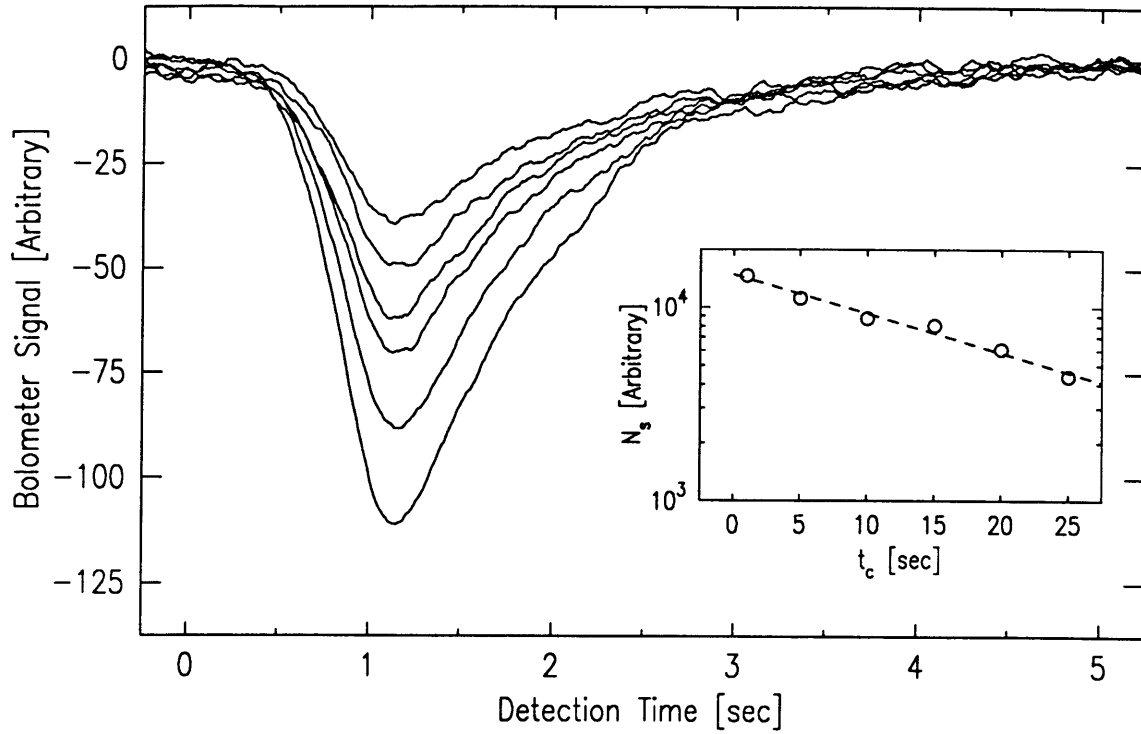
Figure 3-10: Number of 300 μK atoms decays due to contact with the surface. The six signals in order of decreasing area correspond to $t_c = 1, 5, 10, 15, 20,$ and 25 sec respectively. The dashed curve in the inset indicates 21 sec time constant of sticking decay.

long as the surface temperature is well below the energy, 0.6 K, of the ripplon created when a hydrogen atom is absorbed on a superfluid ^{4}He surface [6]. The temperature of the surface was usually held below 85 mK during the contact interval. By varying the surface temperature between 85 mK and 200 mK for some measurements, we found that the influence of surface temperature on the decay due to sticking is negligible.

Chapter 4

Data Analysis

The temperature, T, of the hydrogen atoms used in the experiment is determined from the measured energy distribution. The deviation of the measured energy distribution from the thermal equilibrium energy distribution in Equation 2.3 is discussed in Section 4.1. In addition, the correction to the atom temperature, due to the expansion of the trap when atoms are brought into contact with the surface, is made in the same section.

The sticking probability, $s(T)$, is the ratio of the atoms' decay rate due to sticking to the surface collision rate. The sticking decay rate is determined in Section 4.2 by fitting the data with a function which describes both sticking decay and dipolar electron-spin relaxation decay. The calculation of the collision rate using a Monte Carlo simulation is described in Section 4.3.

The film thickness measurements indicate that as ^{4}He is added to the experimental cell, liquid ^{4}He layer capillarily condensates in the pores of the silver sinter while being sub-saturated elsewhere, reaches saturation, and eventually accumulates into a bulk puddle above the sinter. The analysis of the results of the film thickness measurements is presented in Section 4.4.
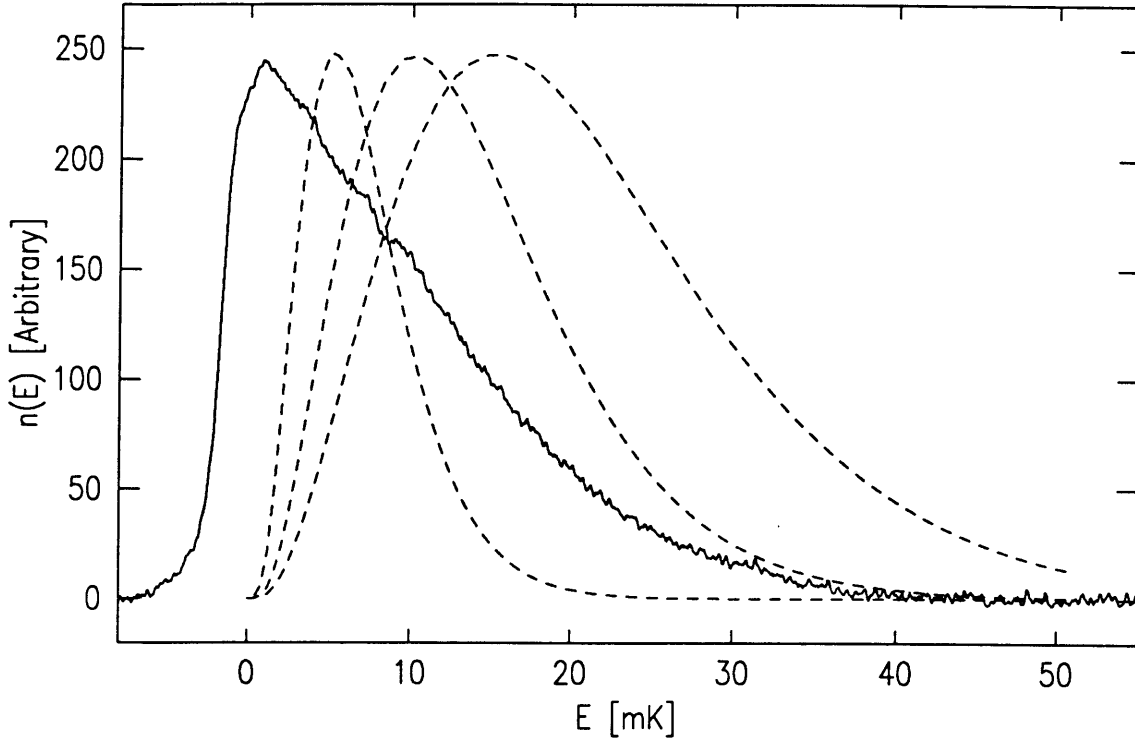
Figure 4-1: Discrepancy between the measured energy distribution with 51-mK trap depth and thermal equilibrium energy distributions in Equation 2.3. The solid curve is the measured energy distribution. The dashed curves are thermal equilibrium energy distributions with $T = 2$, 4, and 6 mK in order of increasing half width.

4.1 Temperature Determination

Atom temperatures in this experiment are associated with ten different trap depths, E_t, ranging from 2.7 mK to 51 mK. The atom temperature can be determined by fitting the measured energy distribution with a thermal equilibrium energy distribution, $n(E)$, as in Equation 2.3. The fit is quite good for the example illustrated in Figure 2-8. However, as E_t becomes deeper, the discrepancy between the measured energy distribution and a thermal equilibrium energy distribution gets worse. In Figure 4-1, the measured energy distribution with $E_t = 51$ mK is compared with $n(E)$ for $T = 2$, 4, and 6 mK. In this figure, either the peak of $n(E)$ shifts away from the measured energy distribution or the half width of $n(E)$ is far narrower than

the measured energy distribution. Possible causes of the discrepancy are non-ergodic behavior of atoms escaping from the trap, and an evaporative cooling effect due to lowering the upper pinch field, when atoms are released from the trap for detection.

Based on the discussions of non-ergodic behavior and the evaporative cooling effect, two methods are employed to determine atom temperature. The average of the results of these two methods, with possible correction due to the expansion of the trap when atom are brought into contact with the surface, is the quoted temperature of the sticking probability.

4.1.1　Non-Ergodic Behavior of Atom Escaping from the Trap

When the upper pinch field is being lowered during detection, not all the atoms with energy above the field barrier can escape from the trap. This non-ergodic behavior is due to atoms with energies greater than the threshold energy that happen to be in orbits which do not bring them to the spatial location from which escape is possible. In an ideal potential that can be completely decomposed into functions containing only either radial or axial coordinate, energy mixing between the radial and axial directions is impossible without the collisions between atoms. Our potential in the trap region (the flat region between the two pinch field barriers) is close to this type with small imperfections. The imperfections can be the coupling between the quadrupole field and the bias field as well as the field inhomogeneity due to trapped flux in the superconducting magnets. Those imperfections surely lead to energy mixing, but are less important in a trap with deeper trap depth. Therefore, the non-ergodic behavior of atoms escaping from a trap with deeper trap depth is expected to be more pronounced.

We model the non-ergodic behavior of atom escaping from the trap by the equa-
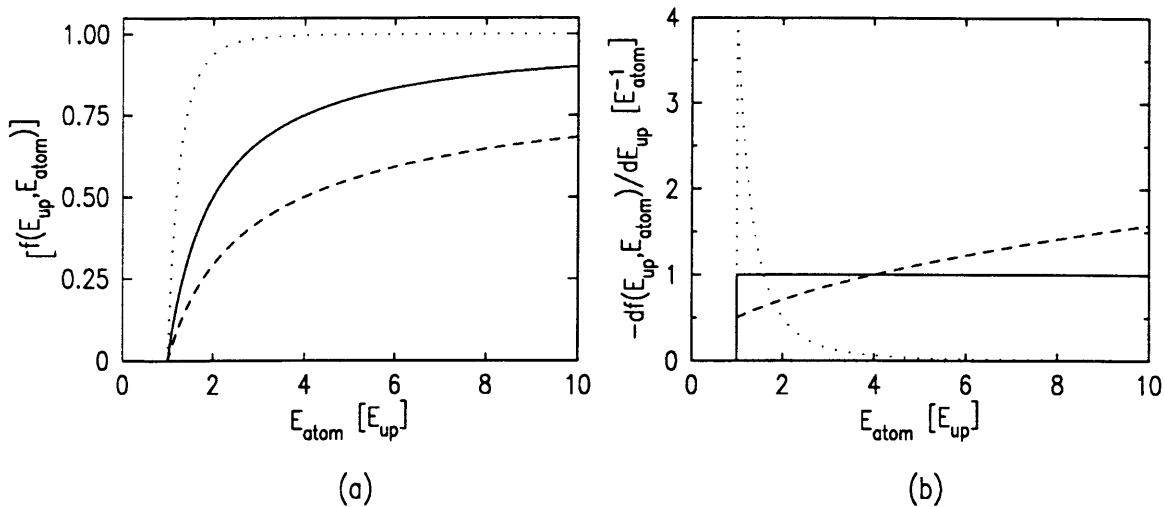
Figure 4-2: The function that describes atom escaping from the trap. The dashed, the solid, and the dotted curves correspond to $\nu = 0.5$, 1, and 4 respectively.

tion,

$$f(E_{up}, E_{atom}) = \begin{cases} 1 - (E_{up}/E_{atom})^{\nu} & \text{for } E_{atom} > E_{up} \\ 0 & \text{for } E_{atom} \leq E_{up} \end{cases} \qquad (4.1)$$

where $f(E_{up}, E_{atom})$ is the fraction of atoms, with total energy E_{atom}, that escapes from the upper pinch barrier E_{up}. ν is a parameter describing the ergodicity. The motion of atoms is completely non-ergodic for $\nu = 0.5$, because $1 - \sqrt{E_{up}/E_{atom}}$ is just the fraction of atoms, with total energy E_{atom}, whose energy in association with the axial motion is larger than E_{up}. On the other hand, $\nu \to \infty$ indicates completely ergodic behavior, since all atoms escape from the trap as soon as the upper pinch barrier is slightly lower than their total energy. In Figure 4-2, $f(E_{up}, E_{atom})$ and $df(E_{up}, E_{atom})/dE_{up}$ are plotted against E_{atom}. The model is compared with the results of a simulation which counts the fraction of atoms that escape from the trap. In the simulation, initial velocities and positions of atoms in the trap, with total energy E_{atom}, are randomly chosen. The trajectory of each atom in the trap is found by solving its equation of motion numerically [40]. The trap is kept static with the

48
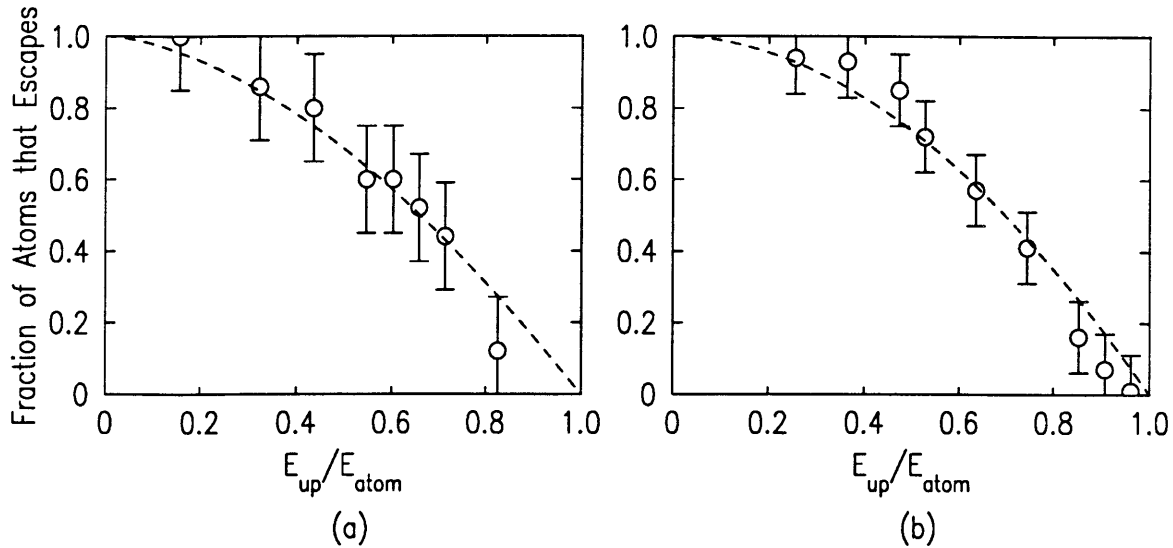
Figure 4-3: Fitting simulation data with $f(E_{up},E_{atom})$ in Equation 4.1. In (a), $E_{atom} = 10$ mK and the fitted $\nu = 1.67$. In (b), $E_{atom} = 50$ mK and the fitted $\nu = 1.92$. In both graphs, the trap profile is the 51-mK-deep one used in this experiment except that E_{up} is varied.

upper pinch barrier at E_{up} during the detection. The simulation time is about 10 times as long as the mean time necessary for an atom to travel between the two pinch barriers and is much shorter than the time of detection. Atoms either remain in the trap or escape during the simulation. The fraction of atoms that escape from the trap is obtained from the statistical average of many such simulations. ν can be determined by fitting the data from the simulation with $f(E_{up},E_{atom})$ as shown in Figure 4-3. The determined ν's are listed in the following table:

trap depth (mK)	2.7	3.2	4.0	5.3	8.0	11	16	27	37	51
E_{atom} (mK)	0.75	0.87	0.87	1.5	1.5	2.0	3.0	5.0	7.0	10
ν	3.88	2.49	2.03	2.03	1.52	1.27	1.85	1.66	1.54	1.67

With the determined ν, the derivative of $f(E_{up},E_{atom})$ with respect to E_{up} is the impulse response function of atom escaping from the trap. Examples of the energy distributions convoluted with the impulse response function, $df(E_{up},E_{atom})/dE_{up}$, are
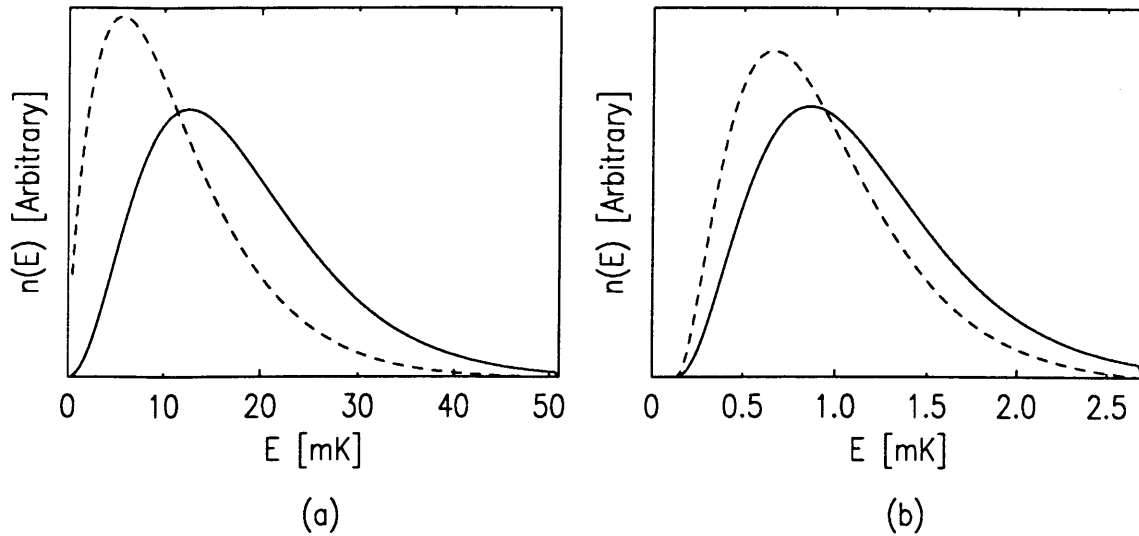
Figure 4-4: Energy distributions affected by non-ergodic behavior of atom escaping from the trap. In (a), the trap depth is 51 mK, $T = 5.1$ mK and $\nu = 1.67$. In (b), the trap depth is 2.7 mK, $T = 310\ \mu$K and $\nu = 3.88$. Both ν's are determined by fitting the simulation data with $f(E_{up}, E_{atom})$ in Equation 4.1. The solid curves are the thermal equilibrium energy distributions in Equation 2.4 and the dashed curves are the energy distributions affected by the non-ergodic behavior. The dashed curve in each graph is normalized to the same area below curve as that of the solid curve.

given in Figure 4-4.

4.1.2   Evaporative Cooling Effect during Detection

When atoms are released from the trap for detection, the upper pinch field is ramped to zero in about 10 sec. For atoms in a deep trap, this ramping time can be so long that the atoms remaining in the trap are evaporatively cooled due to the lowering of the upper pinch field. This is because atoms in a deeper trap are at higher temperature and have a faster inter-atomic collision rate. The thermal equilibrium energy distribution of a deep trap can be distorted by this cooling effect during detection.

The cooling effect due to lowering the upper pinch field during detection can be calculated numerically with the assumption that the trap is always in thermal equilibrium. In the calculation, we keep track of atom loss due to evaporation, dipolar electron-spin relaxation, and release from the trap due to lowering of the upper pinch
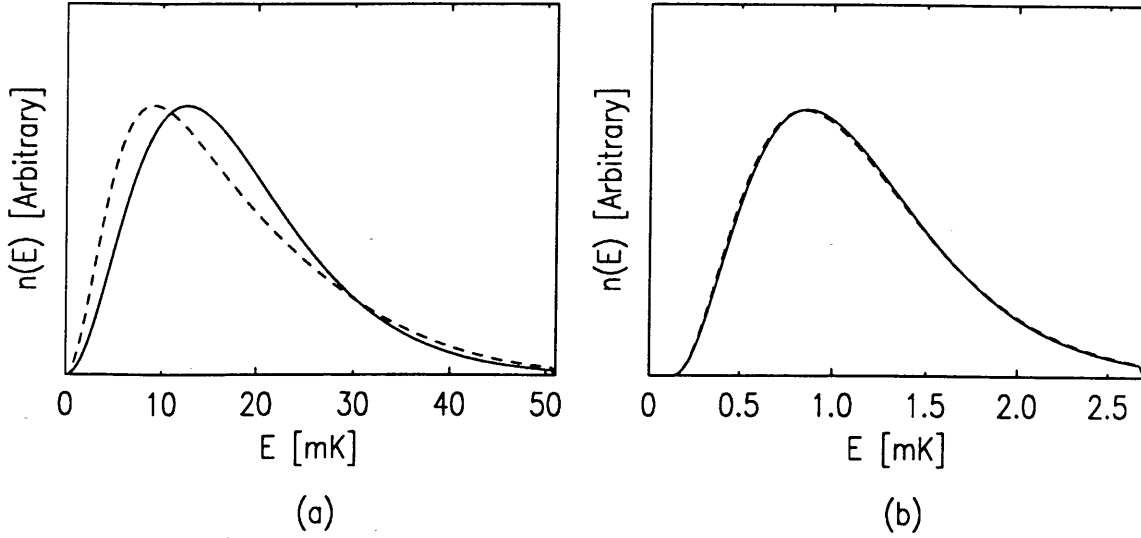
Figure 4-5:   Energy distributions affected by evaporative cooling during the detection. In (a), density on the axis of the trap is 2×10^{13} cm^{-3}, $E_t = 51$ mK, and $T = 5.1$ mK. In (b), density on the axis of the trap is 1×10^{13} cm^{-3}, $E_t = 2.7$ mK, and $T = 310$ μK. The solid curves are the thermal equilibrium energy distributions in Equation 2.4 and the dashed curves are the energy distributions affected by the evaporative cooling effect. All the curves are normalized to the same peak height.

field. We also keep track of the energy carried away by the lost atoms. Moreover, the state of temperature and density of the remaining atoms is determined at every moment during detection. The calculation proceeds iteratively . Given the temperature and the density of the remaining atoms in the trap, the evaporation rate and dipolar electron-spin relaxation rate in the trap are obtained. These rates and the variation of the trap field profile enable the evaluation of atom loss and energy change. The remaining atoms with updated energy reach a new state of temperature and density according to Maxwell-Boltzmann statistics. Then, the evaporation rate and dipolar electron-spin relaxation rate are obtained again. The above iterative process is carried out during a simulated detection and the energy distribution affected by the evaporative cooling is obtained. Two examples of a thermal equilibrium energy distribution compared with a energy distribution affected by the evaporative cooling during the detection are given in Figure 4-5.

4.1.3 Methods of Temperature Determination

The temperature of the trapped atoms is determined by two different methods. The first method assumes that the trapped atoms are in a thermal equilibrium state described by Equation 2.4. It calculates the energy distribution affected by evaporative cooling during detection and then convolutes the outcome with $df(E_{up}, E_{atom})/dE_{up}$. Although ν could be E_{atom}-dependent, only one value of ν is used in $df(E_{up}, E_{atom})/dE_{up}$ for the convolution. This ν is determined from the fitting illustrated in Figure 4-3 with E_{atom} chosen as the energy at the peak of the thermal equilibrium distribution. The result of this convolution is again convoluted with an exponential decay function, which is the impulse response function of the bolometric detection. The time constant of the exponential decay function is about a few tenths of a second and is determined from the decay tail of the measured energy distribution after the upper pinch field is completely zeroed. These distributions are calculated for various temperatures and then compared with the measured distribution. The calculated distribution that most resembles the overall measured distribution sets the temperature of the atoms in the trap. Examples of the above temperature determination are shown in Figure 4-6. The calculated distribution with $T = 5.1$ mK resembles the measured distribution of the trap with $E_t = 51$ mK in Figure 4-6 (a) much more than the thermal equilibrium distributions with $T = 2, 4,$ and 6 mK shown in Figure 4-1. On the other hand, the calculated distribution with $T = 310$ μK in Figure 4-6 (b) is as close to the measured distribution of the trap with $E_t = 2.7$ mK as the one with $T = 300$ μK in Figure 2-8. The results are quite consistent with the pictures described in Section 4.1.1 and 4.1.2.

Although the above method models the measured energy distribution well, the accuracy of the determined temperature is of concern for the following reasons. First of all, the function describing ergodic behavior is not experimentally verified. Secondly, the simulation for escape from the trap not only excludes collisions between atoms but also neglects the imperfections of the trap potential such as azimuthal asymmetry near the pinch fields of the trap and field inhomogeneity caused by trapped flux of the superconducting magnets. Finally, the evaporation rate used in the calculation
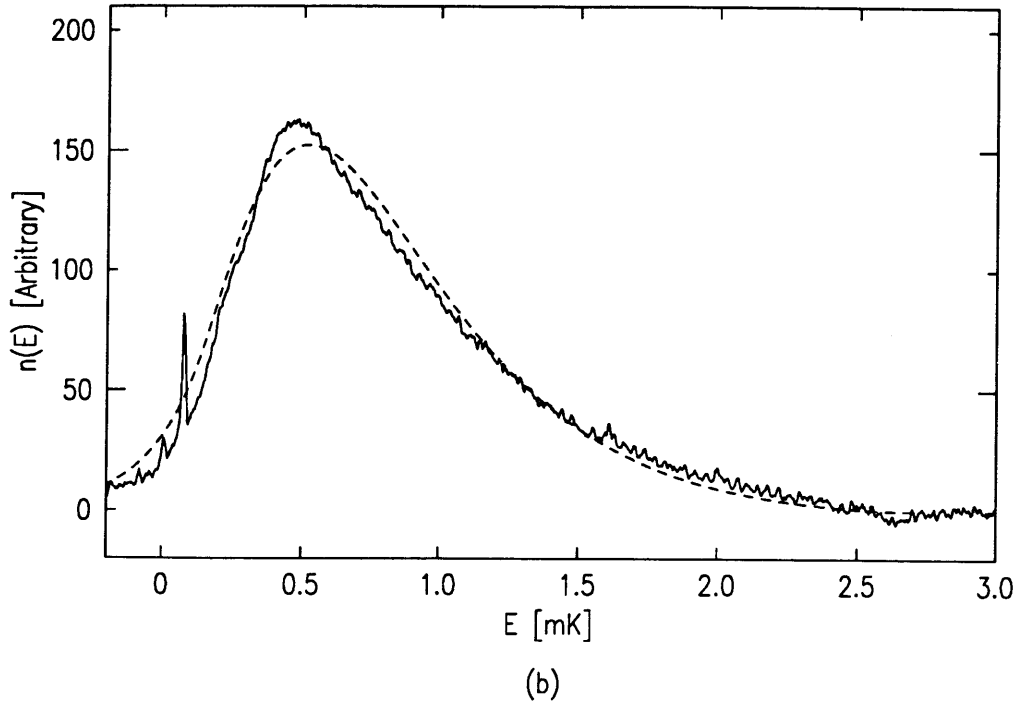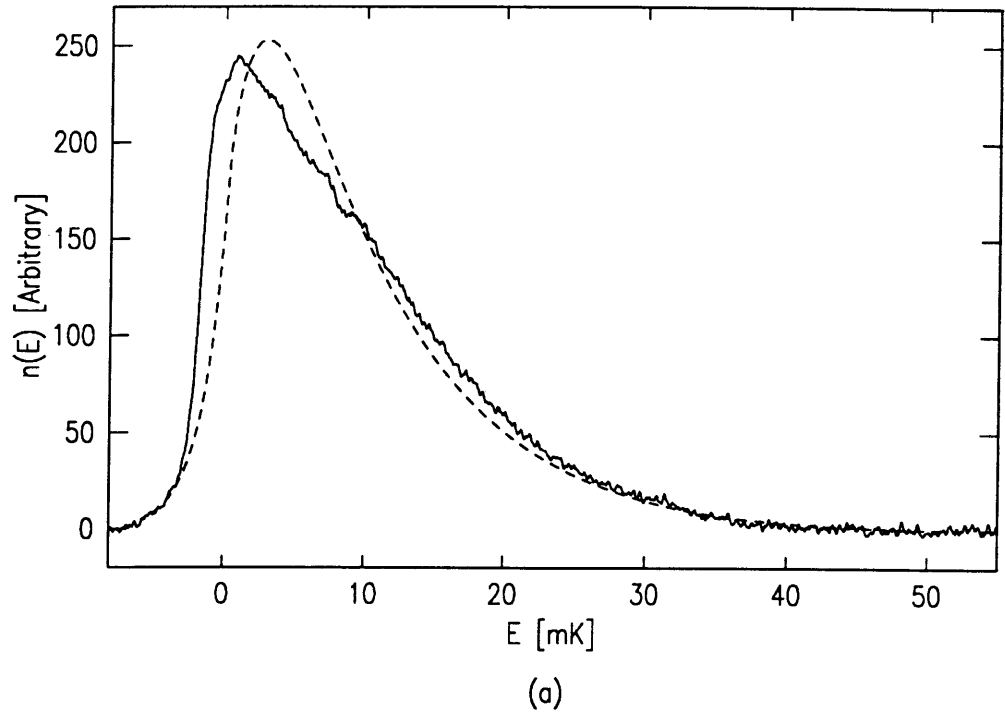
Figure 4-6: Calculated energy distributions with the effects of atom non-ergodic escaping behavior, evaporative cooling during the detection, and response time of bolometric detection. $T = 5.1$ mK and 310 μK, $E_t = 51$ and 2.7 mK, $\nu = 1.67$ and 3.88, and densities on the axis of the trap are 2×10^{13} and 1×10^{13} cm^{-3} in (a) and (b) respectively. The solid curves are the measured distributions, the dashed curves are the calculated distributions .

of the evaporative cooling effect during the detection might not be appropriate when the upper pinch field is close to the temperature of the trapped atoms. Nevertheless, all the above defects makes the determined temperature higher than the actual atom temperature. Therefore, the temperature determined by the first method sets an upper limit on the atom temperature.

The second method of temperature determination sets a lower limit on the atom temperature. This method only compares the high energy tail of the measured energy distribution with that of a thermal equilibrium energy distribution in Equation 2.3 and neglects all the distribution distortion effects mentioned earlier. The reason for the neglect is that the high energy tail of the distribution should be less affected by the distortion effects. The thermal equilibrium distribution for different temperatures is normalized to the same area below the distribution curve as the one of the measured distribution before the comparison. The temperature of the thermal equilibrium distribution whose high energy tail fits best in the comparison with that of the measured distribution is taken as the lower limit of atom temperature. Examples of the above temperature determination are shown in Figure 4-7. The temperature results of both methods are listed in the following table:

trap depth (mK)	2.7	3.2	4.0	5.3	8.0	11	16	27	37	51
method I (mK)	0.31	0.42	0.47	0.52	0.78	1.1	1.2	2.4	3.5	5.1
method II (mK)	0.30	0.35	0.36	0.45	0.65	0.80	1.1	1.9	2.5	3.5

4.1.4 Temperature Correction due to Expansion of the Trap for Surface Contact

When atoms are brought into contact with the surface located at the bottom of the cell, the lower pinch field is turned off as shown in Figure 3-6. The effective length of the trap increases from 18 cm to 25 cm due to the absence of the lower pinch field. Since heating caused by ramping the field is of concern, the time to carry out this

54
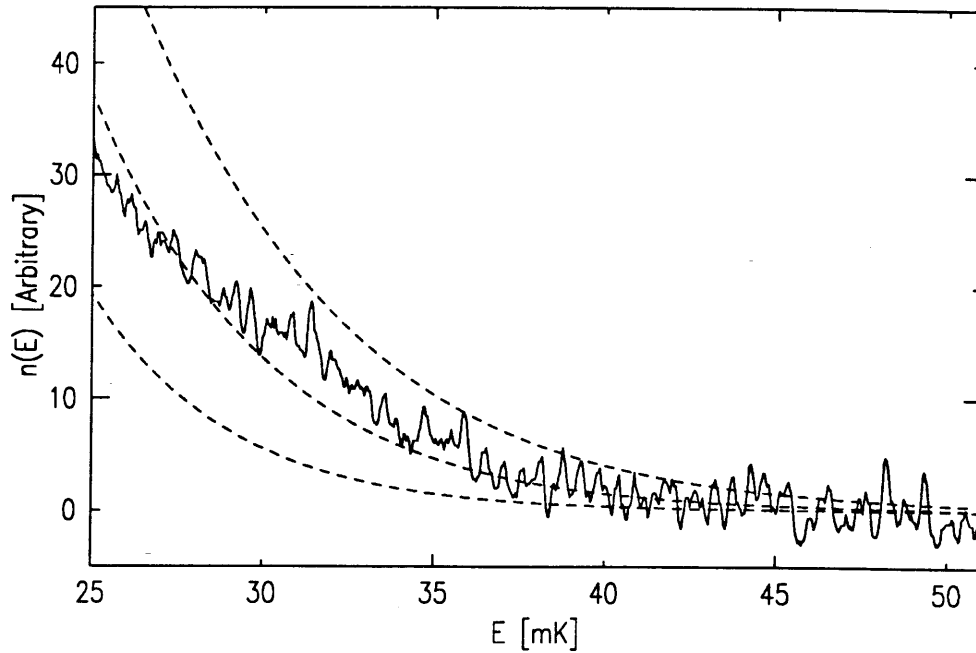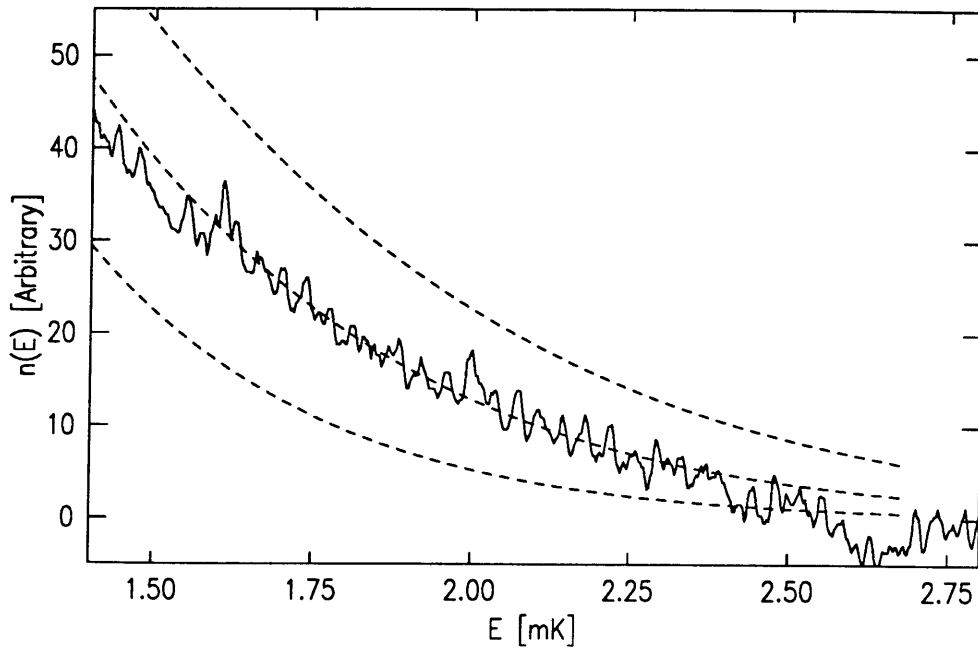
Figure 4-7: Comparisons between the high energy tail of a thermal equilibrium energy distribution and that of the measured energy distribution. In (a), $T = 3.0$, 3.5, and 4.0 mK from the bottom to the top of the dashed curves and $E_t = 51$ mK. In (b), $T = 250$, 300, and 350 μK from the bottom to the top of the dashed curves and $E_t = 2.7$ mK. The solid curves are the measured distributions and the dashed curves are the thermal equilibrium distributions in Equation 2.3.

expansion in the trap volume varies with trap depth. For 300 μK atoms, it is 0.1 sec and on the borderline between free (isothermal) and adiabatic expansion. On the other hand, for 4 mK atoms it is 1 sec, and the expansion is adiabatic.

The temperature change due to adiabatic expansion for our trap is calculated according to conservation of entropy,

$$S = E_{total}/T + \ln(Z) \ .$$ (4.2)

The total energy, E_{total}, and partition function, Z, of atoms with temperature, T, in the trap are given by

$$Z = \iint e^{-H(\vec{r},\vec{p})/k_B T} d^3\vec{p}\, d^3\vec{r}$$ (4.3)

$$E_{total} = \iint H(\vec{r},\vec{p})\, e^{-H(\vec{r},\vec{p})/k_B T} d^3\vec{p}\, d^3\vec{r} \, / \, Z$$ (4.4)

where the integration constraint is $0 \leq H(\vec{r},\vec{p}) \leq E_t$. Before the expansion, the trap profile and the temperature are known, and thus E_{total}, Z, and S can be computed. Since the trap profile is also known after the expansion and the entropy is conserved, one can solve Equation 4.2 numerically to determine the temperature after the expansion.

The temperature change percentage, calculated for the adiabatic expansion, is always less than 5% for all our traps. We only adjusted atom temperatures by the calculated changes for those expansions which are adiabatic. For the rest of the expansions, the calculated changes contribute to the uncertainties of the quoted temperatures.

4.1.5 Summary of Temperature Determination

An average of the two temperatures determined by the methods in Section 4.1.3 is made. This average with the possible correction due to the expansion represents the quoted temperature for the sticking probability. A part of the quoted temperature error bar comes from the difference between these two temperatures. The magnetic

56

field uncertainty of 50 μK and the uncertainty due to the expansion contribute the rest of the quoted error bar. The atom temperatures in this experiment vary between 300 μK and 4 mK, corresponding to thermal de Broglie wavelength between 100 nm and 28 nm, and the temperature error bar varies between 5% and 20% of the atom temperature. A table in Section 4.3 will show both the trap depths and their corresponding atom temperatures.

4.2 Decay Rate Determination

The first step in the analysis procedure for determining the sticking decay rate is to process the raw data collected from the bolometer. The processed data are then integrated to obtain the number of atoms, N_s, remaining after each surface contact interval, t_c. We plot N_s against t_c and fit the data points with a function which describes both sticking decay and dipolar electron-spin relaxation decay in the trap. The decay rate due to sticking is one of the resultant fitting parameters. The above procedure will be discussed in this section.

The raw data of a typical bolometer signal are contaminated by 60 Hz pickup and an oscillation as shown Figure 4-8 (a). The oscillation, which becomes noticeable for superfluid ^{4}He film thicker than 8 nm, is due to third sound (film thickness waves) excited by heating associated with ramping the lower pinch field. Since the raw data are taken digitally, the 60 Hz pickup is eliminated by the Moving Average method. In Figure 4-8 (b), after being eliminating 60 Hz pickup, the data shows the oscillation clearly. The sharp dip area in Figure 4-8 (b) is the signal of the atom flux. Excluding the sharp dip area in the data, the oscillation is fitted with a function summing two sinusoids as in Figure 4-8 (c). The two sinusoids correspond to two heat pulses, one of which is due to turning off the lower pinch field when atoms are brought into contact with the surface, the other of which is due to turning on the same field when atoms are retracted. The data in Figure 4-8 (b) are subtracted from the fitting function (the solid curve in Figure 4-8 (c)). The resultant data from the subtraction are shown in Figure 4-8 (d). Finally integrating the atom flux, the area of the dip in the data,
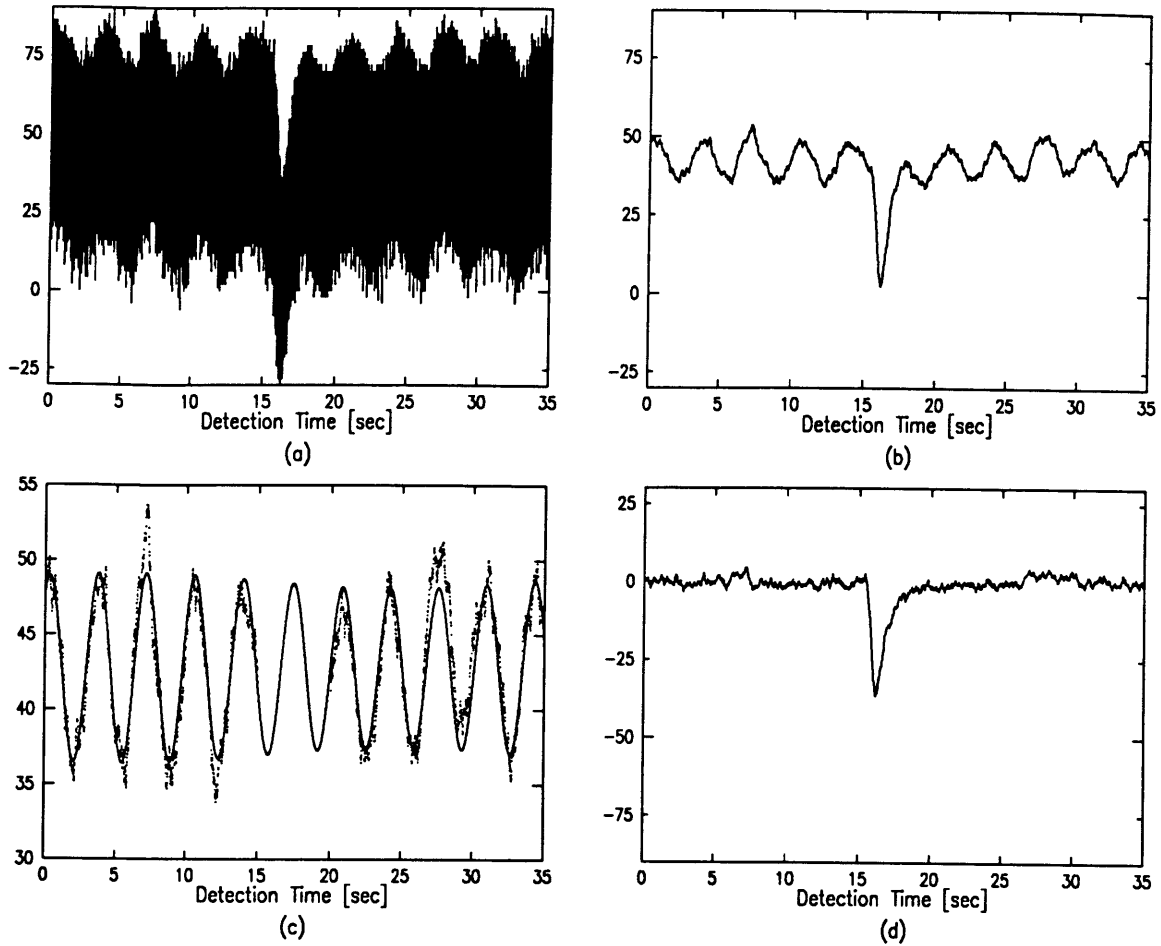
Figure 4-8: The procedure of processing raw data of bolometer signals. The example (300 μK atoms contact bulk helium surface for $t_c = 25$ sec) given here has the worst signal to noise ratio of all analyzed data in this experiment.

gives N_s. Note that N_s is not the absolute number of atoms. However, since the bolometric detection is linear and only the relative numbers of atoms are needed to determine the sticking decay rate, a calibration of N_s is not necessary.

The atoms in the trap always decay due to dipolar electron-spin relaxation, and encounter the sticking decay only when contacting the surface. The timing sequence of an atom-surface collision experimental procedure is shown in Figure 4-9. The
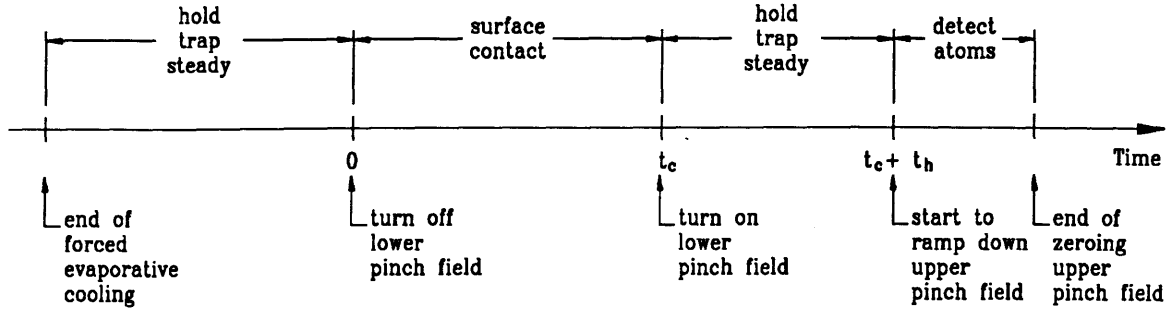
Figure 4-9: The timing sequence of a atom-surface collision experimental procedure.

decay equation of number of atoms, $N(t)$, in the trap is

$$\frac{dN(t)}{dt} = \begin{cases} -g\,\alpha\,N(t)^2 - \tau_s^{-1}\,N(t) & \text{for } 0 < t < t_c \\ -g\,\alpha\,N(t)^2 & \text{for } t_c < t < t_c + t_h \end{cases} \tag{4.5}$$

where g is the dipolar electron-spin relaxation constant mentioned earlier in Section 2.3 and α is a time-independent constant define by Equation 2.9. The above equation leads to

$$N_s(t_c) \equiv N(t_c + t_h) = \frac{N(0)}{(1 + \gamma\tau_s)e^{t_c/\tau_s} + \gamma(t_h - \tau_s)} \tag{4.6}$$

and

$$\gamma = g\,\alpha\,N(0) \ . \tag{4.7}$$

We keep $t_c = 0$ to eliminate τ_s from Equation 4.6 and measure γ experimentally by varying t_h. Once γ is known, the data points of $N_s(t_c)$ versus t_c are fitted with the function in Equation 4.6 and τ_s and $N(0)$ are the only fitting parameters. The decay rate due to sticking, τ_s^{-1}, was therefore determined and the percent uncertainty is around 5% in all measurements.

Since γ is always less than 10% of τ_s^{-1} as well as t_h in this experiment, the decay

function in Equation 4.6 is close to a simple exponential decay function. An example of sticking decay rate determination has been given in the inset of Figure 3-10. Even though the ratio of γ to τ_s^{-1} as well as t_h is about 0.1 in this example, the data points are still pretty close to a line in a semi-log plot as expected.

4.3 Collision Rate Calculation

Consider an idealized geometry such as the one in Figure 2-4 where the upper and lower pinch fields are replaced by perfectly elastic walls. The surface collision rate for an atom on one of the walls is $\bar{v}_z/2L_z$. $\bar{v}_z = \sqrt{2k_BT/\pi m}$ is the mean z-direction speed and L_z is the longitudinal length. The surface collision rate, τ_c^{-1}, in our trap (where confinement along the z axis is due to the helium surface at the bottom and the upper pinch field at the top) calculated by a Monte Carlo simulation is compared with the one of an ideal geometry in the following table:

trap depth	atom temperature	τ_c^{-1} [sec^{-1}]	$\bar{v}_z/2L_z$ [sec^{-1}]
2.7 mK	300 μK	3.9	2.5
3.2 mK	380 μK	4.3	2.8
4.0 mK	420 μK	4.5	3.0
5.3 mK	480 μK	4.8	3.2
8.0 mK	720 μK	5.5	3.9
11 mK	950 μK	6.0	4.5
16 mK	1.2 mK	6.8	4.8
27 mK	2.1 mK	8.4	6.7
37 mK	2.9 mK	9.5	7.8
51 mK	4.1 mK	11	9.3

The deviation of τ_c^{-1} from the collision rate of an ideal geometry is due to the field profile of our trap.

For each atom temperature, the Monte Carlo simulation begins by dividing the energy of the trapped atoms into 20 slices. 50 atoms with random initial velocity and position in the trap are chosen from each energy slice. The trajectory of each atom is simulated in the trap by solving its equation of motion numerically [40]. The trap is in the condition that the lower pinch field is turned off and the helium surface at the bottom of the cell is accessible. The simulation time is long enough such that each atom has several bounces from the surface, but shorter than the sticking time constant. The mean time between two successive surface bounces of the atoms is obtained for each energy slice. The mean times of all the energy slices are then thermally averaged with a Maxwell-Boltzmann distribution. τ_c^{-1} is just the reciprocal of the averaged result. The percent uncertainty of τ_c^{-1} due to the simulation is less than 8% with 0.68 (the probability that a Gaussian random variable is within one standard deviation around the mean) confidence level [41] and the one due to the uncertainty of atom temperature is less than 5%.

4.4 Liquid ^{4}He Film Thickness: Capillary Condensation and Saturation

In Figure 4-10, F is the ^{4}He film thickness on the film burner, viz. bolometer, and A is the amount of ^{4}He added to the experimental cell. The data of F versus A in the figure show three distinct regions of slowly growing, rapidly rising, and slightly varying F, as A is increasing. The different symbols in this figure represent different filling cycles of ^{4}He. The method of the film thickness measurement has been described in Section 3.4.

The region of slowly growing F, as A is increasing, indicates the pores of the sinter are being filled and the superfluid ^{4}He film is sub-saturated. The surface area of the sinter is about 1 m^2 and the apparent surface area of the rest of the cell is 780 cm^2. The total available surface area in the cell is large and the ^{4}He film thickness increases slowly. When ^{4}He film thickness reaches about 3 nm, the sinter with 100 nm pore
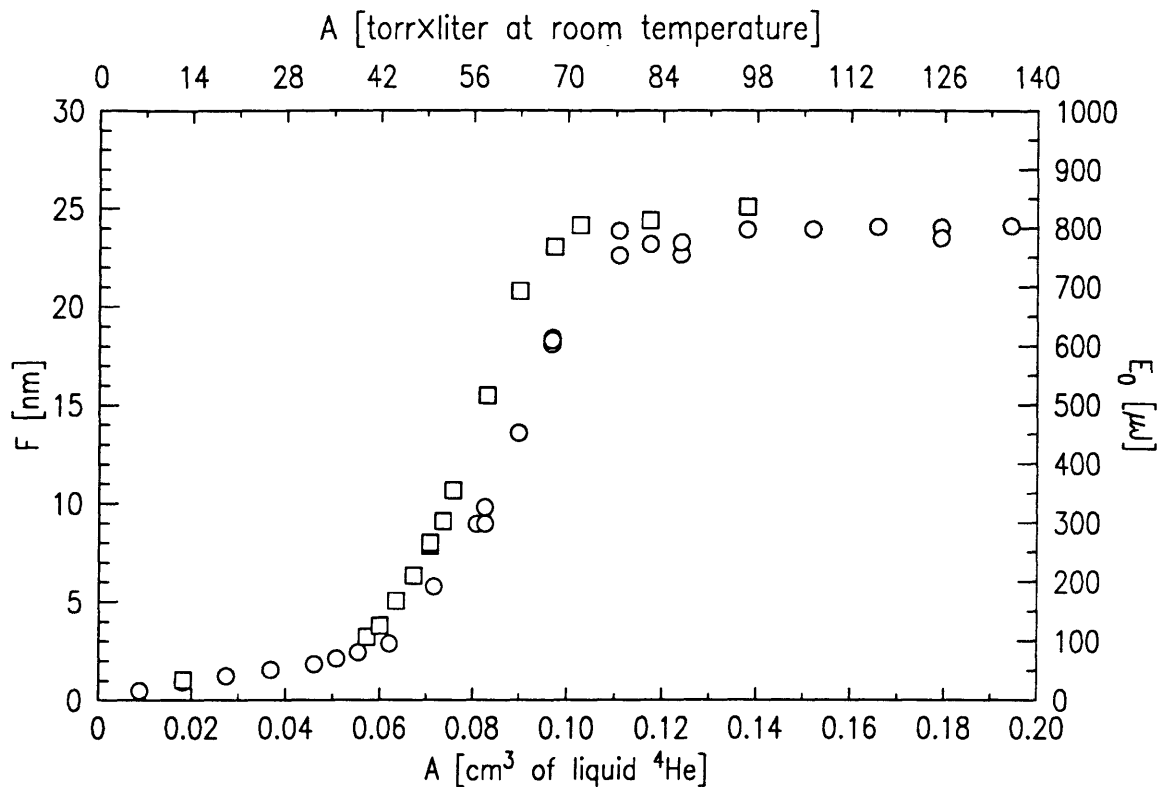
Figure 4-10:   Film thickness on the film burner versus amount of helium
in the cell. The density of liquid ^{4}He used here is 0.15 g/cm^3. The thickness
of saturated ^{4}He film on the film burner is 24 nm. The label on the right
axis is the burning energy required for evaporating the ^{4}He film on the film
burner as defined in Section 3.4.

size suddenly becomes filled. This behavior is capillary condensation and is consistent

with the observation in Reference [43]. In that reference, the critical film thickness

for capillary condensation for ^{4}He on polycarbonate substrate Nuclepore with 80

nm pore diameter is 8 atomic layers (2.8 nm for liquid ^{4}He density 0.15 g/cm^3).

Most importantly, this capillary condensation doesn't happen on the film burner. In

another independent film thickness measurement carried out in the experimental cell

described by Reference [22], no capillary condensation is observed [44]. There was no

porous surface in that experimental cell and the film burner (bolometer) used there

is constructed in the same way with the same material as the one in this experiment.

This fact assures the linearity of the method of film thickness measurement.

After the sinter is filled, the available surface area in the cell decreases dramatically and the superfluid ^{4}He film is still sub-saturated. A small amount of ^{4}He added to the cell increases the film thickness substantially. This behavior is indicated by the region of rapidly rising in F in Figure 4-10. The deviation of the data in this region for the two different ^{4}He filling cycles may be due to the changing surface area due to the accumulation of hydrogen snow.

For sub-saturated ^{4}He film, the thickness of the film above the sinter surface is the same as that on the burner as well as elsewhere in the cell. When the film thickness on the film burner reaches 24 nm, the superfluid ^{4}He film in the cell is saturated. Additional ^{4}He added to the cell only increases the puddle above the sinter and doesn't increase the film thickness elsewhere in the cell. Therefore, the thickness of the liquid layer above the sinter surface is determined volumetrically, after ^{4}He film is saturated in the cell. The saturation is noticed by the region of slightly varying in F in Figure 4-10.

Although the above analysis is consistent, there are some difficulties in the interpretation of the observation. One is that the surface area, deduced from the reciprocal of slope of F versus A in Figure 4-10, of the sinter and that of the cell are 25 to 30 times higher than expected. This could be the consequence of neglecting the surface area created by hydrogen snow and by microscopic structure of the cell wall, excluding the surface area residing in the region of the discharge and the discharge filling line, and underestimating the surface area of the sinter. Moreover, if hydrogen snow and microscopic structure of the cell wall did contribute a fair amount of surface area, then the observed capillary condensation of ^{4}He film would also involve them. Another difficulty is that the geometric surface area of the film burner is about 35 times less than the surface area calculated from E_0 at the saturation in Figure 4-10. This could be due to neglect of the surface area created by the graphite film on the film burner and by the microscopic structure of the quartz plate. Similar problems have been also noticed in other independent experiments, using a same or different film burner, in our group [44, 45]. Nevertheless, the results of the film thickness measurements are justified, since none of the above difficulties affect the linearity of the

measurement method.

The saturation film thickness at the film burner is 24 ± 2 nm. This value is determined from the height of the film burner, 1.8 ± 0.3 cm above the cell bottom, and the equation of film thickness versus height given by

$$d = k/h^{1/n} \ .$$

(4.8)

d is the film thickness, h is the height, and k and n are two parameters determined by the experimental data in Reference [39]. For quartz which is one of the two film burner surfaces, $k = 228 \pm 2$ Åcm$^{1/n}$ and $n = 3.08 \pm 0.3$ at $T = 2.10$ K. For gold which is plated on the other surface of the film burner, $k = 323 \pm 3$ Åcm$^{1/n}$ and $n = 3.91 \pm 0.15$ at $T = 2.13$ K. Saturation film thickness of 24 nm equates the burning energy of 800 μJ of the film thickness measurement. This calibrates the thickness measurements at sub-saturated film coverage and contributes a percent uncertainty of 10% to quoted film thickness. Another uncertainty comes from the reproducibility of the measurements. Summing both uncertainties, the percent error bar for the quoted film thickness is about 20%.

Chapter 5

Results and Conclusions

We have measured the sticking probability of atomic hydrogen on superfluid ^{4}He for atom temperatures between 300 μK and 4 mK. Data are presented for 0.5 nm to 1 mm thick ^{4}He films on a silver sinter substrate. Based on the analysis in the previous chapter, the percent uncertainties of the data are 18% in the sticking probability, 5% to 20% in temperature, and 20% in ^{4}He film thickness. The measurements were performed over a period of 8 weeks. The helium film was completely removed and reformed a few times during that period. The reproducibility of the measured sticking probabilities is consistent with the estimated uncertainty.

The results of the sticking probability measurements for bulk ^{4}He provide the first experimental evidence for universal quantum reflection and are in good agreement with recent theories [10, 11, 9]. The observed the film thickness dependence of the sticking probability demonstrates the influence of the van der Waals-Casimir force due to the substrate.

5.1   Evidence for Universal Quantum Reflection

Sticking probability data on bulk ^{4}He for hydrogen atom temperatures of 300 μK to 4 mK are presented in Figure 5-1. The two most recent theoretical calculations from Carraro and Cole (referred to as CC) [10, 11] and Hijmans, Walraven, and
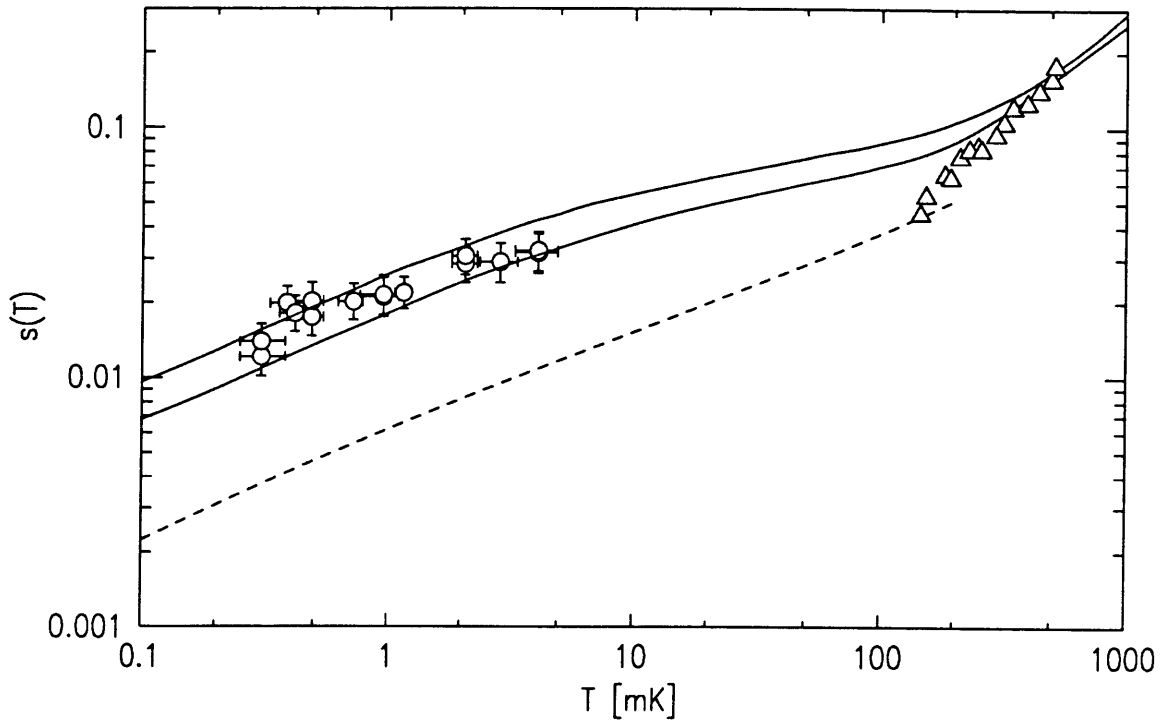
Figure 5-1: Sticking probability of atomic hydrogen on bulk liquid ^{4}He. O: this work; △: Berkhout et al. [12, 13]; solid curves: calculation of CC [11] (upper curve, E_B = 1.1 K; lower curve, E_B = 1.0 K); dashed curve: calculation of HWS [9] (E_B = 1.0 K).

Shlyapnikov (referred to as HWS) [9] are also shown as two solid curves and a dashed curve respectively. For the dashed curve, sticking probability was originally calculated as a function of $E_\perp$, the kinetic energy associated with the motion perpendicular to the helium surface. The adjustment $s(T) = (\sqrt{\pi}/2)\ s(E_\perp = k_B T)$ is made, which applies when $s(E_\perp) \propto \sqrt{E_\perp}$. The differences between the two theories will be discussed in a later paragraph. The binding energy, E_B, of a hydrogen atom on liquid helium surface assumed in the calculation of the upper solid curve is 1.1 K, whereas that of the lower solid curve as well as the dashed curve is 1.0 K. Several recent measurements of E_B by various techniques give values ranging from 0.89 K to 1.15 K [46, 47, 48, 49, 50]. The temperature axis in the figure is extended to include the higher temperature data of Berkhout et al. [12, 13].

66

The temperature dependence of the data of this work is in good agreement with the curves of both theoretical calculations. The calculations of both CC and HWS predict that $s(T) \propto \sqrt{T}$ as T approaches zero and the curve of $s(T)$ is a little flattened in the temperature regime of this work. The slope of our data can be fit by a temperature exponent of 0.30 ± 0.03 over this limited temperature regime. Hence, the onset of universal quantum reflection is observed as predicted. On the other hand, the theories are not consistent with the higher temperature data of Berkhout et al. [12, 13]. Those data have linear temperature dependence for 145 mK $< T <$ 526 mK. The discrepancy between the high temperature data and the theories implies that the current theories are not adequate to describe surface sticking at the higher temperature regime.

The magnitude of the data of this work is in excellent agreement with the values calculated by CC. The calculations of CC and HWS employ the first-order distorted-wave Born approximation (DWBA) to determine the sticking probability at bulk ^{4}He (CC's calculation might include corrections to the "distorted" wave function of the incident atom). The interaction potentials between hydrogen atom and liquid ^{4}He used in CC and HWS are somewhat different. The potentials of CC and HWS are plotted in Figure 5-2. The hydrogen-liquid ^{4}He potential in the calculation of CC has the following asymptotic behaviors:

$$V_{CC}^b(z) \longrightarrow \mu_0/(1 + e^{\beta z}) \qquad \text{for } z \ll 4 \text{ Å} \tag{5.1}$$

$$\longrightarrow -(C_3/z^3)\,\gamma(z) \qquad \text{for } z \gg 25 \text{ Å} \tag{5.2}$$

μ_0 ($= 37$ K) is the penetration energy of hydrogen atom into liquid helium. β ($= 0.568$ and 0.587 Å^{-1}) is an adjustable parameter, which determines E_B (1.0 and 1.1 K respectively). C_3 ($= 223$ KÅ^3) is the coefficient of van der Waals potential. Finally, $\gamma(z)$ is the retardation correction approximated by

$$\gamma(z) = (1 + z/\lambda)^{-1} \tag{5.3}$$
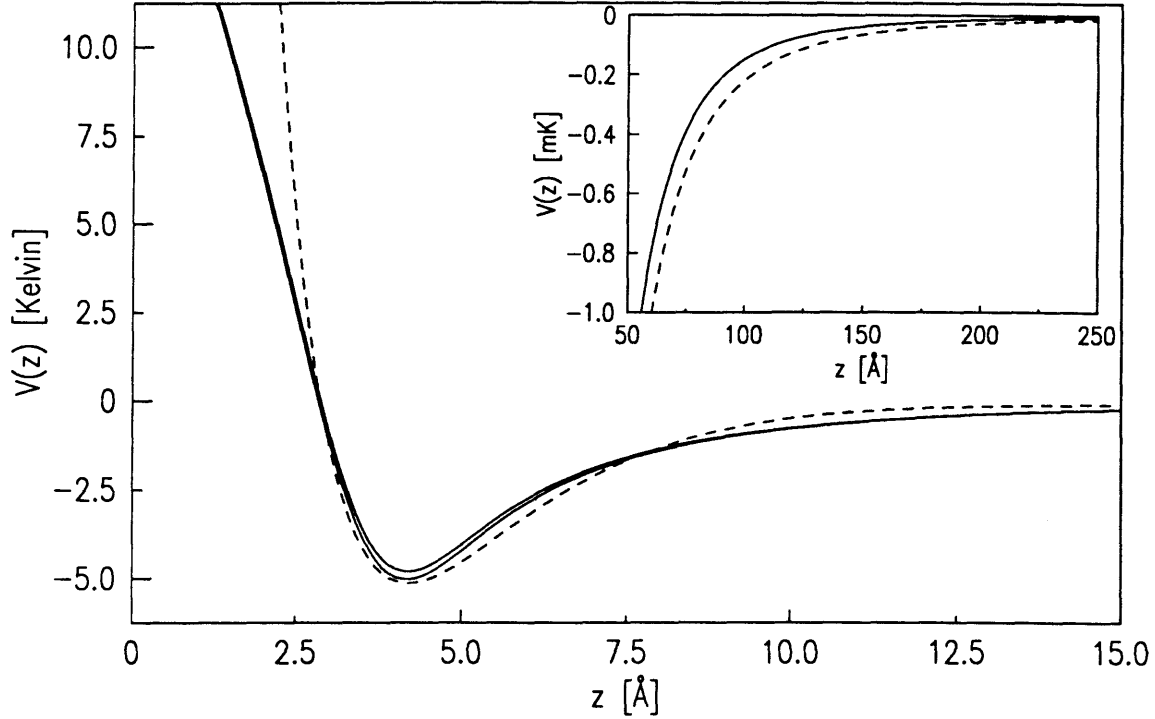
Figure 5-2: Interaction potential between hydrogen atom and liquid ^{4}He. The upper and lower solid curves are the potentials in CC's calculation with $E_B = 1.0$ and 1.1 K respectively. The dashed curve is the potential in HWS's calculation with $E_B = 1.0$ K.

where the characteristic length, λ, is 200 Å. On the other hand, the hydrogen-liquid ^{4}He potential in the calculation of HWS behaves asymptotically like

$$V^b_{HWS}(z) \longrightarrow \epsilon[e^{2\beta(z-z_0)} - 2e^{\beta(z-z_0)}] \qquad \text{for } 0.1 \text{ Å} \leq z \ll 13 \text{ Å} \qquad (5.4)$$

$$\longrightarrow -C_3/z^3 \qquad \text{for } z \gg 13 \text{ Å} \qquad (5.5)$$

where the short range potential is just a Morse potential and $C_3 = 219.7$ KÅ^3. In the Morse potential, $\epsilon = 5.14$ K, $\beta = 0.52$ Å^{-1}, and $z_0 = 4.2$ Å. The above parameters correspond to $E_B = 1.0$ K. It is difficult to define μ_0 in $V^b_{HWS}(z)$, because $V^b_{HWS}(z)$ diverges as $z \rightarrow 0$ according to Equation 12 of Reference [9]. The behavior and strength of both long-range attractive potentials of CC and HWS are very close, except that the retardation effect is neglected in HWS's potential. As for the short-

range repulsive potentials, that of HWS is much stronger than that of CC. The functional forms of both short-range potentials are quite different.

To summarize, the temperature dependence of the bulk data in this experiment is consistent with the onset of $s(T) \propto \sqrt{T}$ behavior. The magnitude of the data are in excellent agreement with the theoretical calculation of CC. The work is the first experimental evidence for believing in universal quantum reflection.

5.2 Demonstration of the Influence of the van der Waals-Casimir Force

As the ^{4}He film on the surface becomes thinner, the van der Waals-Casimir force due to the substrate underneath the ^{4}He film has more influence on impinging hydrogen atoms. The effect is clearly shown in Figure 5-3. Four different symbols from the top to the bottom of the figure correspond to film thickness of 0.5 nm, 3 nm, and 10 nm and a bulk layer. Not only does the temperature exponent of the sticking probability varies over the range of film thicknesses, but the magnitude of $s(T)$ changes dramatically. For comparison, the sticking probability of 300 μK atoms on bulk ^{4}He is 0.013, whereas on 0.5-nm thin ^{4}He film it is 0.66. This 50-fold change in sticking probability is quite striking.

In Figure 5-3, the 10-nm data were taken when the sinter surface was fully covered by the liquid helium. The 3-nm data correspond to the pores of the sinter just being filled and the 0.5-nm data correspond to open pores. This behavior of the superfluid ^{4}He film has been described in Section 4.4. The dotted line is a representative of the data in a previous experiment [16]. These data were taken in the situation that the surface was an epoxy substrate covered by approximately 6-nm-thick superfluid ^{4}He film. There is little doubt that the previous results are influenced by the substrate. The curves of CC [10, 11] and HWS [9] in Figure 5-3 were originally calculated as a function of $E_\perp$. Since both curves are pretty flat, the adjustment of $s(T) = s(E_\perp = k_B T)$ is made, which applies when $s(E_\perp)$ depends only weakly on $E_\perp$. Two solid curves
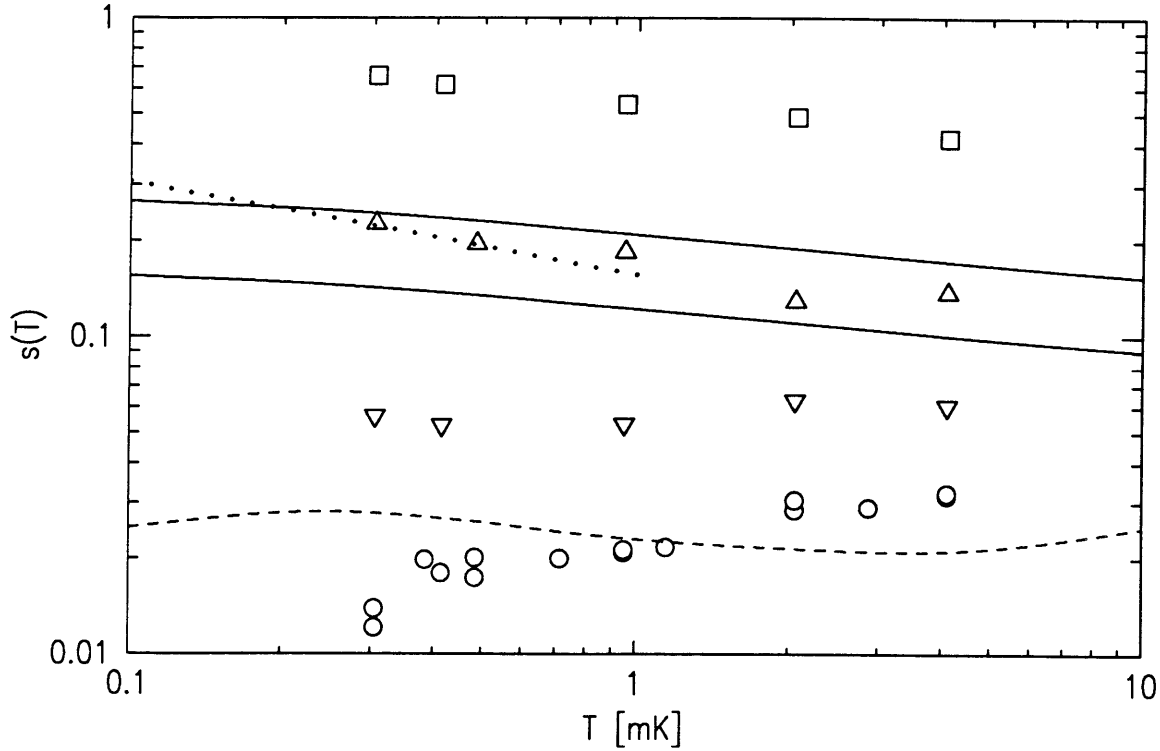
Figure 5-3: Sticking probability of atomic hydrogen on liquid ^{4}He covered surface. □: 0.5 nm; △: 3 nm; ▽: 10nm; ○: bulk limit; dotted line: the results from a previous experiment [16]; solid and dashed curves: calculations for 5-nm thickness of CC [11] ($C_s = 5000$ KÅ^3) and HWS [9] ($C_s = 4600$ KÅ^3) respectively. The temperature and sticking probability uncertainties of the data are the same as those in Figure 5-1.

are calculated by CC [10, 11] with the same potential and parameters. The difference between the two is that the lower solid curve is obtained using the first-order DWBA method, while the upper one is obtained using first-order DWBA with corrections to the "distorted" wave function of the incident atom. The dashed curve is calculated by HWS [9] with first-order DWBA. The interaction between hydrogen atoms and the sintered silver substrate in the experiment might not be properly represented by the theories and the roughness of the surface in the experiment might influence the results. Thus the lack of quantitative agreement between the data and the calculations is to be expected. However, the qualitative consistency of the temperature dependence is encouraging.
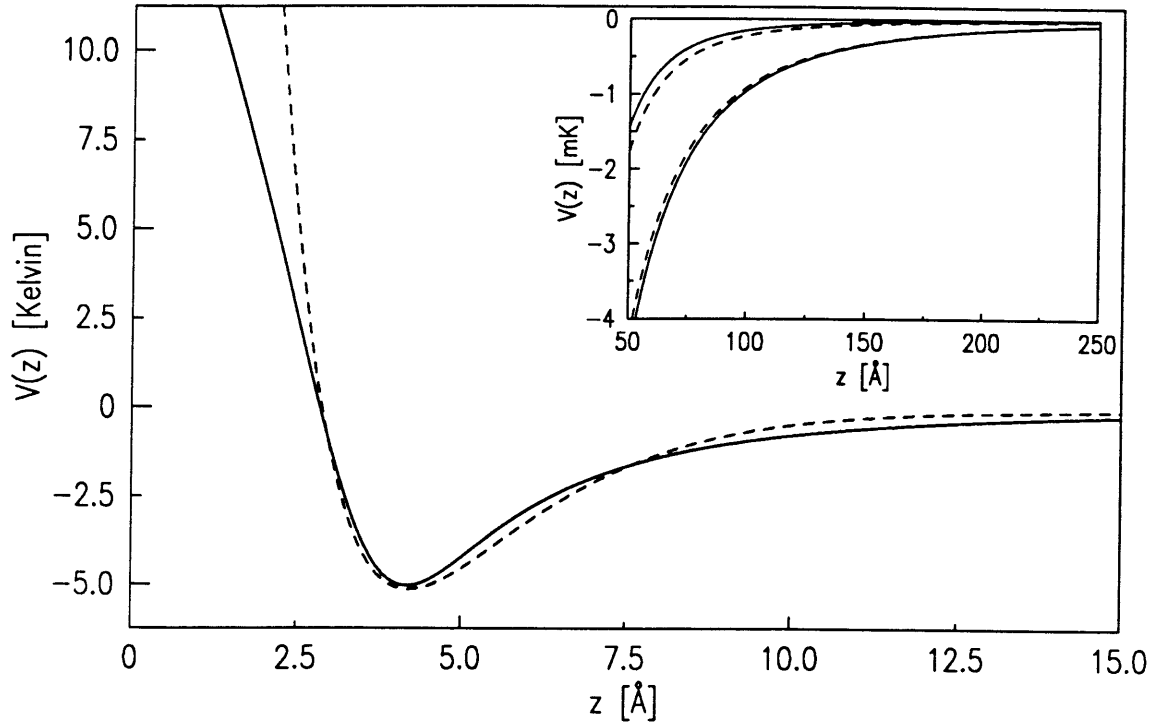
Figure 5-4: Interaction potential between hydrogen atom and liquid ^{4}He covered surface. Solid curves: $V_{CC}^s(z,d)$ (upper and lower ones for $d = \infty$ and 5 nm respectively); dashed curves: $V_{HWS}^s(z,d)$ (upper and lower ones for $d = \infty$ and 5 nm respectively).

The potentials used by CC ($V_{CC}^s(z,d)$) and HWS ($V_{HWS}^s(z,d)$) for the calculations of the above curves with thickness d are shown in Figure 5-4. Both potentials contain a term corresponding to hydrogen-substrate van der Waals-Casimir potential. The finite thickness effect of ^{4}He layer is also considered in $V_{CC}^s(z,d)$ and $V_{HWS}^s(z,d)$ by subtracting part of hydrogen-liquid helium potential. The hydrogen-substrate van der Waals-Casimir potential in $V_{CC}^s(z,d)$ has the same functional form as Equation 5.2. For $V_{CC}^s(z,d)$, C_s (hydrogen-substrate's C_3) = 5000 KÅ^3, $\beta = 0.587$ Å^{-1}, and the rest of parameters are the same as those in $V_{CC}^b(z)$. On the other hand, the hydrogen-substrate van der Waals-Casimir potential in $V_{HWS}^s(z,d)$ is

$$- g(\lambda/[z+d]) \; C_s \; / \; (z+d)^3 \qquad (5.6)$$

71
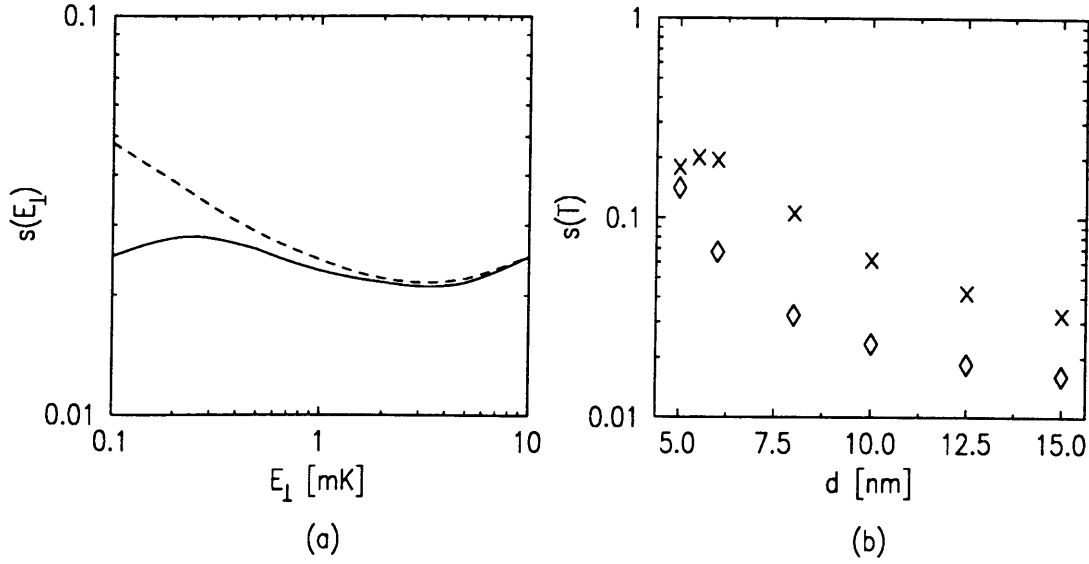
Figure 5-5: Retardation effect on sticking probability. In (a), the solid and dashed curves are predicted by HWS [9], with and without retardation effect respectively, for $d = 5$ nm. In (b), the diamonds and crosses are predicted by CC [11], with and without retardation effect respectively, for $T = 100$ μK.

where $g(\lambda/[z+d])$, the retardation correction, is given by

$$g(1/x) = \left[1 - (1 + x)\,e^{-2x}\right]/x \quad . \tag{5.7}$$

For $V_{HWS}^{s}(z,d)$, $C_{s} = 4600$ KÅ^{3}, λ (characteristic retardation length) $= 200$ Å, and the rest of parameters are the same as those in $V_{HWS}^{b}(z)$.

It is interesting to examine the retardation effects reported in both calculations. Figure 5-5 (a) shows the sticking probability versus temperature with and without retardation effect. Figure 5-5 (b) shows the sticking probability versus thickness with and without retardation effect. The retardation effects on the temperature exponent (shown in Figure 5-5 (a)) and the magnitude (shown in Figure 5-5 (b)) of the sticking probability are significant. Figure 5-6 presents the measured film thickness dependence of the sticking probability for 300 μK atoms. At the moment, there are no calculations available for a direct comparison between the experimental
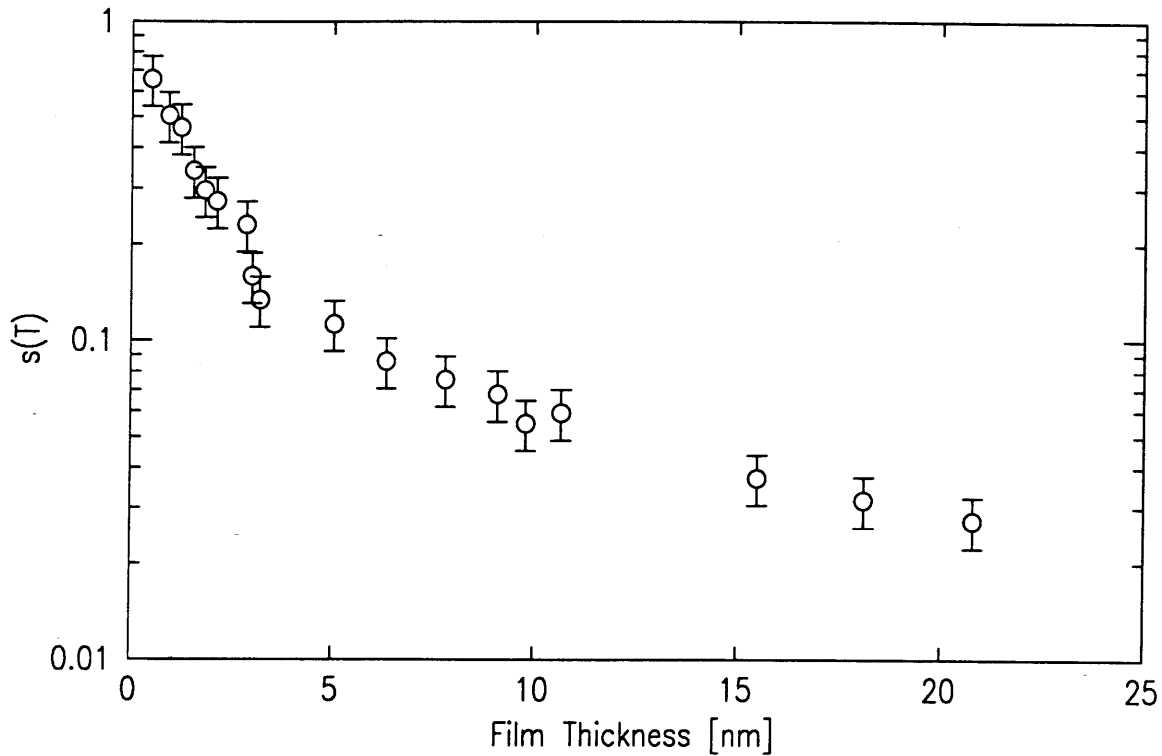
Figure 5-6: Film thickness dependence of the sticking probability on film thickness at a temperature of 300 μK.

data and theories. Nevertheless, with more accurate film thickness measurements on a better characterized substrate, the Casimir-Polder force could be determined from data similar to that shown in Figure 5-6.

5.3   Summary

The sticking probability data of atomic hydrogen on a silver sintered surface covered by superfluid ^{4}He have been presented. The atom temperatures are between 300 μK and 4 mK, corresponding to thermal de Broglie wavelengths between 100 and 28 nm. The magnetic field uncertainty for a shallow-depth trap limits atom temperature at the low end, and the heating caused by ramping high magnetic fields prevents us from measuring the sticking probability at a higher temperature. The thickness of the ^{4}He film on the top of the surface varies from 0.5 nm to a bulk puddle. The silver sinter

underneath the ^{4}He film assures that the temperature of the film does not rise due to hydrogen recombination heat generated during the sticking events. The choice of the sintered substrate limits the accuracy of our measurements of the sticking probability at the lower film coverages. On the other hand, the data for bulk liquid ^{4}He coverage are not affected by the substrate.

The bulk data provide the first experimental evidence for universal quantum reflection. A comparison between the bulk data and the theories of both CC and HWS implies that the sticking probability is very sensitive to the hydrogen-liquid ^{4}He short-range repulsive force. For the same binding energy, the sticking probability due to the potential with a stronger short-range repulsive force (the dashed curve in Figure 5-2) is about 5 times less than that with a weaker one (the upper solid curve in Figure 5-2). This suggests that the sticking probability measurements for bulk coverage not only examine the quantum nature of atom-surface collisions, but also provide an excellent opportunity to understand and model the short-range interaction.

The thin film data clearly demonstrate the van der Waals-Casimir force due to the substrate and the 300 μK thin film data have a 50-fold change in the sticking probability from the corresponding bulk data. The theories of CC and HWS also predict considerable differences in the thin film sticking probability depending on whether one includes the retardation effect in the hydrogen-substrate potential. This suggests that the thin film sticking probability measurements can provide a means of studying the Casimir-Polder force under controlled conditions.

Further study of universal quantum reflection in a lower temperature or energy regime and improved measurements of the thickness dependence of the sticking probability on a well-understood substrate are the natural directions to proceed. A brief discussion of these will be given in the next chapter. In conclusion, as is demonstrated by the results of this work, sticking probability measurements provide a great opportunity to explore interesting physics.

Chapter 6

Design of Future Experiment

This work has been well received [51]. It is the first step toward a detailed understanding of universal quantum reflection and determination of the Casimir-Polder force. In this chapter, techniques and apparatus for the next generation experiments will be suggested.

The sticking probability of atomic hydrogen on bulk ^{4}He behaving $\sqrt{T}$ or $\sqrt{E_\perp}$ for T or $E_\perp$ ranging from 30 to 300 μK is predicted by the theories [10, 11, 9]. $E_\perp$ is the the kinetic energy associating the motion perpendicular to the helium surface. The predictions are shown in Figure 6-1. Although we have difficulty producing atom temperatures below 100 μK, it is feasible to have $E_\perp$ as low as 30 μK (0.5 Gauss) by some modifications of the current trap. The technique as well as the modifications of the trap for producing 30 μK $E_\perp$ is presented in Section 6.1. Atoms this slow would significantly extend our ability to study universal quantum reflection.

The above technique can be also generalized to measure the sticking probability at energies higher than 4 mK. Measuring the temperature dependence of the sticking probability over a wider temperature range with bulk ^{4}He will allow one to characterize and quantify the hydrogen-liquid helium short-range interaction. The interaction potential between atomic hydrogen and a liquid ^{4}He covered surface can be written
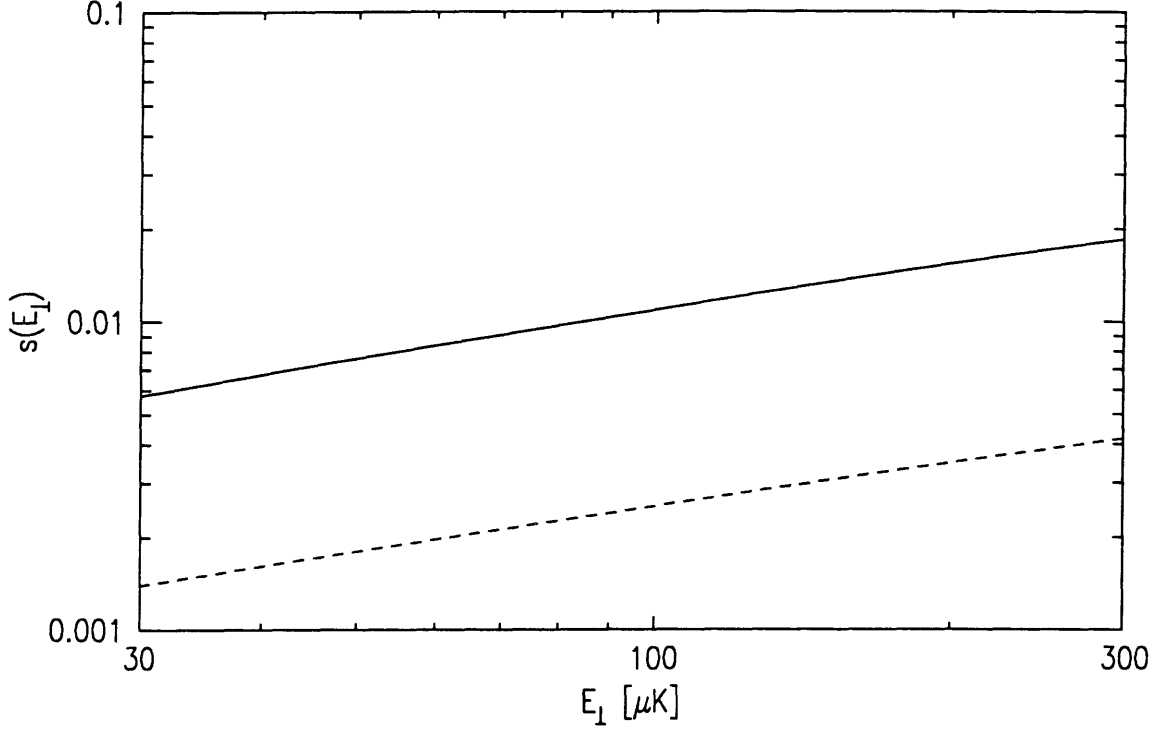
Figure 6-1: Prediction of universal quantum reflection for sticking probabilities of 30 to 300 μK hydrogen atoms on bulk ^{4}He. Solid curve: CC (E_B = 1.1 K) [10, 11]; dashed curve: HWS (E_B = 1.0 K) [9].

as

$$V(z,d) = V^{sr}_{H-He}(z) - \gamma(z)\,C_3\,(1/z^3 - 1/(z+d)^3) - \gamma(z+d)\,C_s/(z+d)^3 \qquad (6.1)$$

where a small number, which prevents $V(z,d)$ from diverging at $z = 0$, in the denominator of the van der Waals potential is omitted. $V^{sr}_{H-He}(z)$ is the hydrogen-liquid helium short-range repulsive potential, $\gamma(z)$ is the retardation correction, d is the film thickness, and C_3 and C_s are the hydrogen-liquid helium and hydrogen-substrate van der Waals coefficients respectively. The liquid ^{4}He surface facing incoming atoms is at $z = 0$. For $C_3 \ll C_s$,

$$V(z,d) \approx V^{sr}_{H-He}(z) - \gamma(z+d)\,C_s/(z+d)^3 \qquad (6.2)$$

76

Therefore, with adequate knowledge of V^{sr}_{H-He}, measurements of the thickness dependence of the sticking probability on liquid ^{4}He film covered surface is equivalent to study of the Casimir-Polder force. The thickness dependence of the sticking probability is only affected by the long-range potential and, on the other hand, the magnitude of the sticking probability is influenced by both short-range and long-range potentials. Identifying the Casimir-Polder force from the thickness dependence seems less argumentative than that from the magnitude. For the film thicknesses where the retardation effect becomes dominant, more theoretical effort should be expended to find the difference in thickness-dependent exponent of the sticking probability depending on whether one includes $\gamma(z)$. The best candidate for the substrate may be an alkali metal, because of its strong polarizability in dipole-dipole interaction. Any other material with well-understood van der Waals coefficient would also be a good choice. In any case, the surface structure of the substrate should be well controlled. A high fidelity film burner is proposed in Section 6.2. This easily-implemented device can be suitable for measuring film thickness with reasonable accuracy. Once quantitative data of the sticking probability versus film thickness are obtained, the Casimir-Polder force will be demonstrated clearly.

6.1 Method of Obtaining Atoms with Low Incident Energy on a Surface

The basic idea of the technique of producing $E_\perp$ as low as 30 μK is to separate the lower field barrier of the trap and the magnetic field at liquid ^{4}He surface by a fixed amount, 0.5 Gauss, for 30 μK. The uncertainty, $\Delta E_\perp$, is controlled by the decrement in the low pinch field when atoms are released from the trap. $\Delta E_\perp$ can be as small as 0.1 Gauss (7 μK). This is illustrated in Figure 6-2. The apparatus that realizes the technique is shown in Figure 6-3. Most of it is the same as used in this experiment, except that the lower end of the cell is extended. The extension, surrounded by two new copper-wire-wound solenoids outside the vacuum can, is in
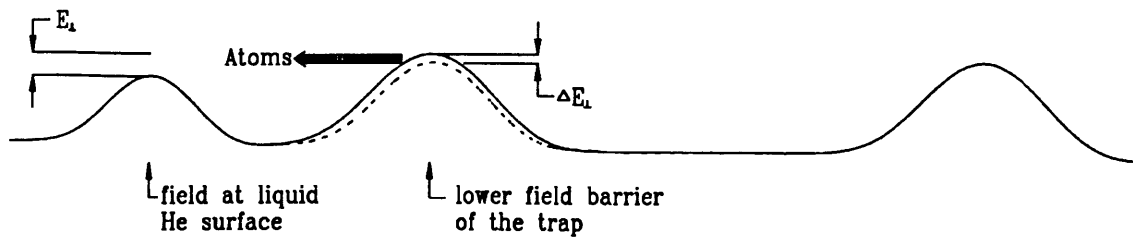
Figure 6-2:   Sketch for producing 30 μK atom-surface collisions.

a small diameter. The new solenoids are expected to generate magnetic fields less than 15 Gauss. Through careful design, the new solenoids might be made small enough that the extension can have the same diameter as the rest of the cell. One of the solenoids is the surface solenoid which generates the field at ^{4}He surface. The other is the differential solenoid and generates a part of the lower field barrier of the trap. The lower field barrier of the trap is now the sum of the field generated by

Figure 6-3:   Apparatus for producing 30 μK atom-surface collisions.

Time t_1 —— 60s —— t_2 — 1s — t_3 — 5s — t_4 — 1s — t_5 ······

Upper Pinch Filed [Gauss]	50.5	↘	15.5
Lower Pinch Filed [Gauss]	50	↘	15
Differential Filed [Gauss]	0.5		↘ 0.4 ↗ 0.5
Surface Filed [Gauss]		15	

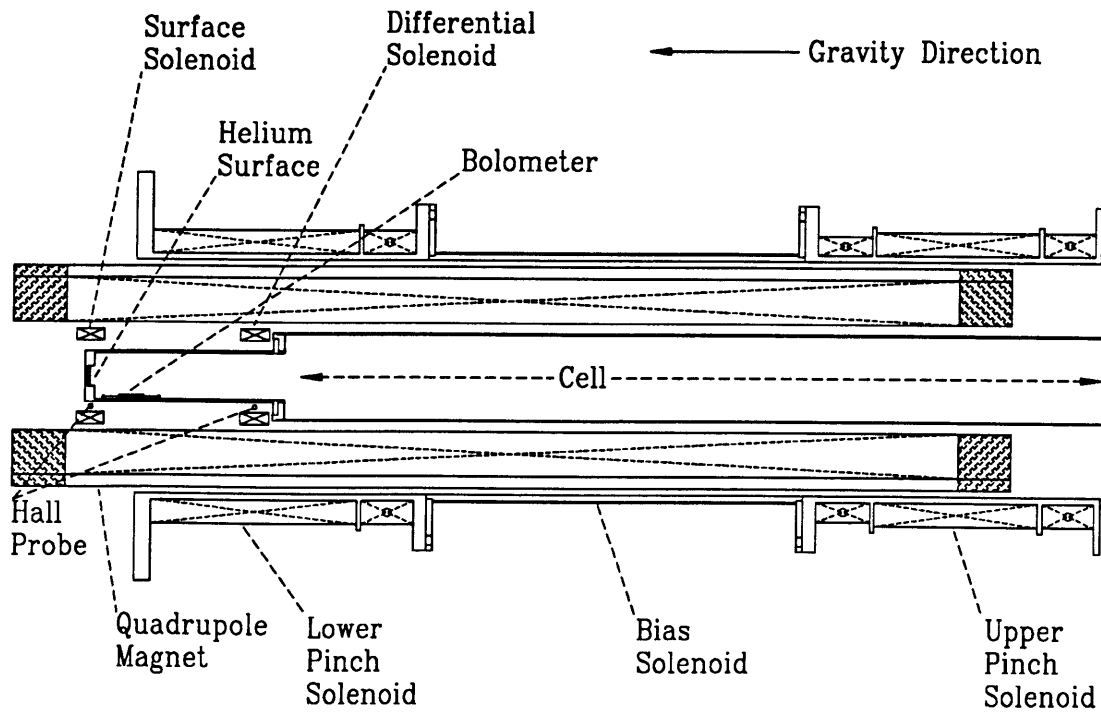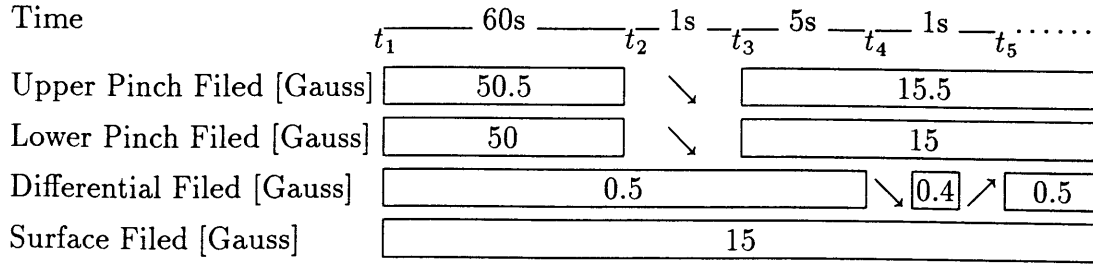Figure 6-4: Example of the experimental procedure for producing 30 μK atom-surface collisions. The number in each box indicates the strength of the magnetic field in Gauss during the time period of the length of the box and the arrow denotes the field is ramping down or up.

the differential solenoid and the field generated by lower pinch solenoid. Two on-site Hall probes measure the field at the liquid ^{4}He surface and the lower end of the trap. From earlier experience, magnetic field measurements with 0.1 Gauss precision at liquid helium temperature are achievable. All the above modifications of the current apparatus can be implemented without difficulties.

An example of the experimental procedure for producing 30 μK $E_\perp$ is described in Figure 6-4 and the time evolution of the energy distribution of the remaining atoms in the trap is shown in Figure 6-5. At t_1, the trap is just at the end of a forced
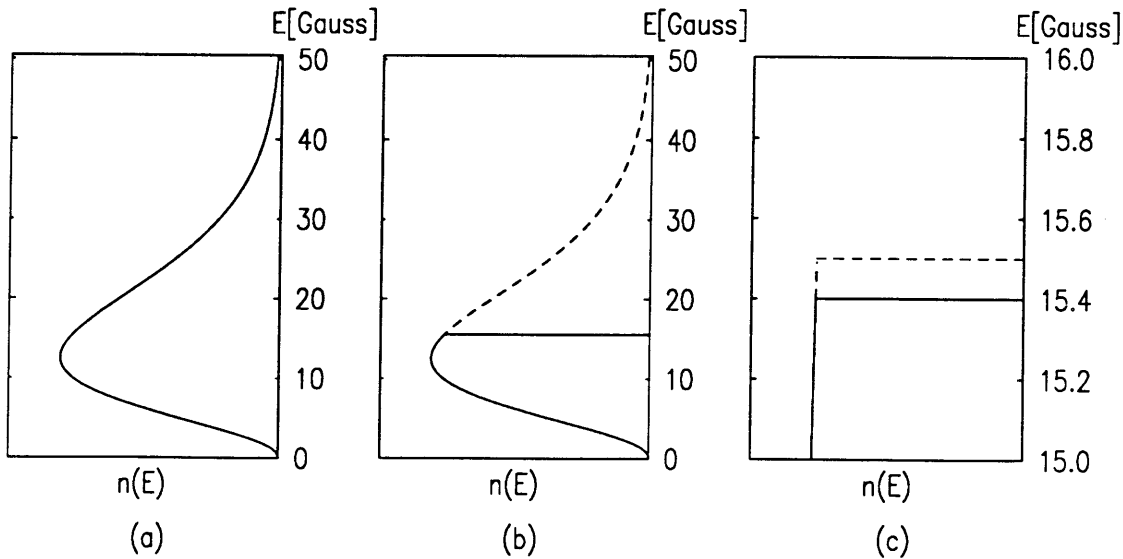

Figure 6-5: Time evolution of the energy distribution of the remaining atoms in the trap for producing 30 μK atom-surface collisions. (a) $t_1 < t < t_2$; (b) $t_3 < t < t_4$; (c) $t_5 < t$.

evaporative cooling. The trap depth is about 50 Gauss (3.4 mK). After a typical 60-sec period, the trapped atoms should reach thermal equilibrium with a temperature of about 340 μK at t_2. At this temperature, the energy at the peak of the energy distribution is around 850 μK. In the next 1 sec after t_2, the trap depth is lowered to a value (close to the energy at the peak of the distribution), say 15.5 Gauss (1 mK). At t_3, the lower pinch solenoid contributes 15 Gauss to the lower field barrier of the trap, and the differential solenoid contributes 0.5 Gauss. During the interval between t_3 and t_4, the atoms with energy higher than the trap depth escape and the remaining atoms haven't reached a new equilibrium. Therefore, a fair number of trapped atoms are just below the trap depth at t_4. The surface field is always kept at 15 Gauss, which is 0.5 Gauss (30 μK) below the trap depth. Now, the differential solenoid is instantaneously lowered by 0.1 Gauss at t_4 and risen back at t_5. All the trapped atoms within this 0.1 Gauss energy slice are released from the trap through a tiny orifice at the lower end of the trap during this 1 sec interval between t_4 and t_5. These atoms are just like a jet coming out of a container and most of their energy is associated with the motion perpendicular to the liquid ^{4}He surface. They bounce back and forth between the liquid helium surface and the lower barrier of the trap yet have only $E_\perp = 30$ μK when they reach the surface. Upon sticking to the surface, atoms will recombine and the recombination energy will be detected by the bolometer. Therefore, one is able to measure the sticking probability of 30 μK hydrogen atoms on bulk ^{4}He from the decay curve of the bolometer signal. Signal averaging, increasing the ratio of the quadrupole field to the pinch field to enhance atom flux, and shortening the distance between the surface and the lower end of the trap to decrease atom traveling time can be used to improve the signal to noise ratio.

The above method of slicing the energy distribution of trapped atoms will not only produce $E_\perp$ as low as 30 μK but also minimize the heating due to ramping the fields. The third sound oscillation caused by the heat pulse was one of the major noise sources in the raw data of this experiment. Furthermore, this method can also be employed to measure the sticking probability at atom energies higher than 4 mK. The great advantage is that the field barrier doesn't need to be zeroed for surface
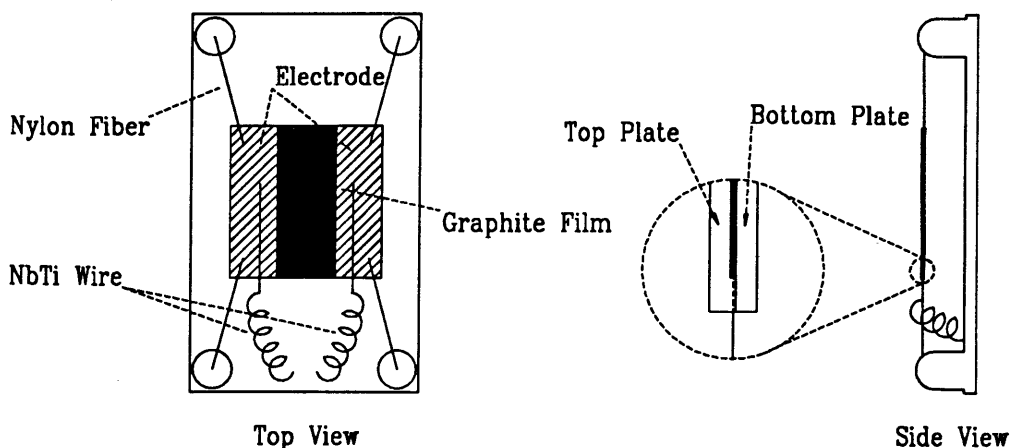
Figure 6-6: Structure of a high fidelity film burner.

contact, so a lot of heating is avoided.

6.2 High Fidelity Film Burner

A High fidelity film burner is one that can be used to determine a ^{4}He film thickness directly from burning energy measurements. As the plots shown in Figure 3-8 and Figure 3-9 indicate, the signal to noise ratio of the burning energy measurements is excellent. However, the burning energy of a film burner, as well as the resonance frequency of a crystal quartz microbalance and the capacitance of a liquid-^{4}He-filled capacitor, only measure the volume of liquid ^{4}He film. In order to determine the film thickness directly, the surface structure (surface area) of any thickness measurement device has to be well characterized. A high fidelity (Hi-Fi) film burner can be designed to meet the above requirement.

A possible design for a Hi-Fi film burner is shown in Figure 6-6. It is similar to the one used in this work, except that a top plate is added. The top and bottom plates sandwich the graphite film, the electrodes, the nylon suspending fibers, and the NbTi wires. In the current design, these sandwiched elements are uncovered and contribute to the uncertainty of the surface area of the film burner. This uncertainty can be eliminated in this design provided the two plates of a Hi-Fi film burner

81

have a well-characterized surface structure. Super-polished quartz is an example of a material with this property. Unlike a bolometer (the current film burner) for very sensitive energy measurements, a film burner is not required to have low heat capacity. Therefore, the choice of the plate material should be more flexible. The construction procedure of a Hi-Fi film burner can be the one described in Section 3.3, with the top plate grown by MBE technique or placed by other methods in the last step. As a precaution, the surface area of a finished Hi-Fi film burner can be examined by SEM or another more advanced, but non-destructive, microscopic imaging method.

Although the measurement precision of a Hi-Fi film burner might not be as good as that of a quartz microbalance, the measurement accuracy of a Hi-Fi film burner is suitable for studying the thickness dependence of the sticking probability. Furthermore, by placing a couple of Hi-Fi film burners at the different heights in the experimental cell, the height dependence of ^{4}He saturation film thickness can be verified. This provides a cross-check on the film thickness, as determined by the burning energy. Most importantly, a Hi-Fi film burner could be developed in a short time scale with our current knowledge of the film burning measurement and our current technique of constructing a film burner.

6.3 Suggestions

Ultracold atomic hydrogen is a unique species. Along with Bose-Einstein condensation and high precision hydrogen 1S-2S spectroscopy, one should be able to achieve some short-term physics goals with ultracold atomic hydrogen . The proposed $s(E_\perp)$-versus-$E_\perp$ study of atomic hydrogen with $E_\perp$ as low as 30 μK on bulk liquid ^{4}He and the film thickness dependence of the $s(E_\perp)$ are possible short-term physics goals. The method and device described in this chapter require no dramatic innovations. They can be developed in parallel with our major experiments and the proposed experiment can be carried out in one-and-one-half years. In return for this small investment, one could increase our understanding of universal quantum reflection and, possibly, demonstrate clearly the Casimir-Polder force.

Bibliography

[1] G. Iche and P. Nozières, "A simple stochastic description of desorption rates," *Journal de Physique*, vol. 37, p. 1313, 1976.

[2] T. Martin, R. Bruinsma, and P. Platzman, "Quantum reflection in the presence of dissipation," *Physical Review B*, vol. 38, p. 2257, 1988.

[3] D. P. Clougherty and W. Konh, "Quantum theory of sticking," *Physical Review B*, vol. 46, p. 4921, 1992.

[4] T. R. Knowles and H. Suhl, "Sticking coefficient of atoms on solid surfaces at low temperatures," *Physical Review Letters*, vol. 39, p. 1417, 1977.

[5] T. Martin, R. Bruinsma, and P. M. Platzman, "Critical-like behavior in quantum adsorption," *Physical Review B*, vol. 39, p. 12411, 1989.

[6] D. S. Zimmerman and A. J. Berlinsky, "The sticking probability for hydrogen atoms on the surface of liquid ^{4}He," *Canadian Journal of Physics*, vol. 61, p. 508, 1983.

[7] Y. Kagan and G. Shlyapnikov, "On the possibility of attaining the Bose-condensation region in spin-polarized atomic hydrogen at ultra-low temperatures," *Physics Letters*, vol. 95A, p. 309, 1983.

[8] V. V. Goldman, "Kapitza conductance between gaseous atomic hydrogen and liquid helium," *Physical Review Letters*, vol. 56, p. 612, 1986.

[9] T. W. Hijmans, J. T. M. Walraven, and G. V. Shlyapnikov, "Influence of the substrate on the low-temperature limit of the sticking probability of hydrogen atoms on He films," *Physical Review B*, vol. 45, p. 2561, 1992.

[10] C. Carraro and M. W. Cole, "Comment: H atom sticking to He and He films," *Physical Review Letters*, vol. 68, p. 412, 1992.

[11] C. Carraro and M. W. Cole, "Role of long-range forces in H sticking to liquid He," *Physical Review B*, vol. 45, p. 12930, 1992.

[12] J. J. Berkhout, E. J. Wolters, R. van Roijen, and J. T. Walraven, "Vanishing sticking probabilities and enhanced capillary flow of spin-polarized hydrogen," *Physical Review Letters*, vol. 57, p. 2387, 1986.

[13] J. J. Berkhout and J. T. Walraven, "Scattering of hydrogen atoms from liquid-helium surfaces," *Physical Review B*, vol. 47, p. 8886, 1993.

[14] J. Helffrich, M. P. Maley, M. Krusius, and J. C. Wheatley, "Measurement of thermal accommodation of spin-polarized hydrogen on a saturated ^{4}He film at 0.18-0.4 K," *Physical Review B*, vol. 34, p. 6550, 1986.

[15] J. Helffrich, M. P. Maley, and M. Krusius, "Thermal accommodation of spin-polarized hydrogen on liquid-He surfaces below 0.25 K," *Physical Review B*, vol. 42, p. 2003, 1990.

[16] J. M. Doyle, J. C. Sandberg, I. A. Yu, C. L. Cesar, D. Kleppner, and T. J. Greytak, "Hydrogen in the submillikelvin regime: sticking probability on superfluid ^{4}He," *Physical Review Letters*, vol. 67, p. 603, 1991.

[17] W. C. Stwalley and L. H. Nosanow, "Possible "new" quantum systems," *Physical Review Letters*, vol. 36, p. 910, 1976.

[18] R. M. Panoff and J. W. Clark, "Ground-state phases of polarized deuterium species," *Physical Review B*, vol. 36, p. 5527, 1987.

[19] T. J. Greytak and D. Kleppner, "Lectures on spin-polarized hydrogen," in *New Trends in Atomic Physics* (G. Grynberg and R. Stora, eds.), (Amsterdam), p. 1127, Les Houches Summer School, North-Holland, 1982.

[20] I. F. Silvera and J. T. M. Walraven, "Spin-polarized atomic hydrogen," in *Progress in Low Temperature Physics Volume X* (D. F. Brewer, ed.), ch. 3, p. 139, Elsevier, 1986.

[21] J. M. Doyle, *Energy Distribution Measurements of Magnetically Trapped Spin Polarized Atomic Hydrogen: Evaporative Cooling and Surface Sticking*. PhD thesis, Massachusetts Institute of Technology, 1991.

[22] J. C. Sandberg, *Research toward Laser Spectroscopy of Trapped Atomic Hydrogen*. PhD thesis, Massachusetts Institute of Technology, 1993.

[23] W. Kolos and L. Wolniewicz, "Variational calculation of the long-range interaction between two ground-state hydrogen atoms," *Chemical Physics Letters*, vol. 24, p. 457, 1974.

[24] Y. Kagan, I. A. Vartanyants, and G. Shlyapnikov, "Kinetics of decay of metastable gas phase of polarized atomic hydrogen at low temperatures," *Sov. Phys. JETP*, vol. 54(3), p. 590, 1981.

[25] A. Lagendijk, I. F. Silvera, and B. J. Verhaar, "Spin exchange and dipolar relaxation rates in atomic hydrogen: Lifetimes in magnetic traps," *Physical Review B*, vol. 33, p. 626, 1986.

[26] H. T. C. Stoof, J. M. V. A. Koelman, and B. J. Verhaar, "Spin-exchange and dipole relaxation rates in atomic hydrogen: Rigorous and simplified calculations," *Physical Review B*, vol. 38, p. 4688, 1988.

[27] H. F. Hess, G. P. Kochanski, J. M. Doyle, N. Masuhara, D. Kleppner, and T. J. Greytak, "Magnetic trapping of spin-polarized atomic hydrogen," *Physical Review Letters*, vol. 59, p. 672, 1987.

[28] N. Masuhara, J. M. Doyle, J. C. Sandberg, D. Kleppner, and T. J. Greytak, "Evaporative cooling of spin-polarized atomic hydrogen," *Physical Review Letters*, vol. 61, p. 935, 1988.

[29] H. Hess, "Evaporative cooling of magnetically trapped and compressed spin-polarized hydrogen," *Physical Review B*, vol. 34, p. 3476, 1986.

[30] DuPont Company, Wilmington, Delaware.

[31] Puratronic, 99.9985%; Johnson Matthey Catalog Co., Inc., Ward Hill, Massachusetts.

[32] Q. Li, C. H. Watson, R. G. Goodrich, D. G. Haase, and H. Lukefahr, "Thick film chip resistors for use as low temperature thermometers," *Cryogenics*, vol. 26, p. 467, 1986.

[33] Vacuum Metallurgical Co., Ltd., Japan; North American distributor Ulvac North America Corp., Kennebunk, Maine.

[34] V. Keith and M. G. Ward, "A recipe for sintering submicron silver powder," *Cryogenics*, vol. 24, p. 249, 1984.

[35] P. A. Busch, S. P. Cheston, and D. S. Greywell, "Properties of sintered-silver heat exchangers," *Cryogenics*, vol. 24, p. 445, 1984.

[36] Emerson & Cumming Inc., Canton, Massachusetts.

[37] Acheson Colloids Company, Port Huron, Michigan.

[38] R. A. Sherlock, "Frequency response optimization of the constant temperature detector system — a detailed root-locus analysis," *Journal of Physics E: Scientific Instruments*, vol. 17, p. 386, 1984.

[39] D. Hemming, "Helium film profile on a gold and a quartz substrate," *Canadian Journal of Physics*, vol. 49, p. 2621, 1971.

[40] Code provided by J. M. Doyle.

[41] N. P. Buslenko, D. I. Golenko, Y. A. Shreider, I. M. Sobol, and V. G. Sragovich, *The Monte Carlo Method; the Method of Statistical Trials* (Yu. A. Shreider, ed.) translated from Russian by G. J. Tee. Pergamon Press, 1966. In Eq. 1.6, $\delta \leq \sigma\sqrt{\frac{1}{\epsilon N}}$, where δ, σ^2, ϵ, and N are error of the simulation result, confidence level on error, and variance and number of independent measurements respectively. This inequality follows Chebyshev's theorem, the proof of which can be found in Ref. [42].

[42] B. V. Gnedenko, *The Theory of Probability* translated from Russian by B. D. Seckler, p. 239. Chelsea Publishing Company, 1967.

[43] D. T. Smith, K. M. Godshalk, and R. B. Hallock, "Adsorption and capillary condensation of ^{4}He on nuclepore: third-second and capacitance measurements," *Physical Review B*, vol. 36, p. 202, 1987.

[44] C. L. Cesar, D. G. Fried, and A. D. Polcyn, private communication.

[45] M. J. Yoo, private communication.

[46] M. Morrow, R. Jochemsen, A. J. Berlinsky, and W. N. Hardy, "Zero-field hyperfine resonance of atomic hydrogen for $0.18 \leq T \leq 1$ K: the binding energy of H on liquid ^{4}He," *Physical Review Letters*, vol. 46, p. 195, 1981. "Errata," *Physical Review Letters*, vol. 47, p. 455, 1981. $E_B = 1.15$ K.

[47] A. P. M. Matthey, J. T. M. Walraven, and I. F. Silvera, "Measurement of pressure of gaseous H↓: Adsorption energies and surface recombination rates on helium," *Physical Review Letters*, vol. 46, p. 668, 1981. $E_B = 0.89$ K.

[48] R. W. Cline, T. J. Greytak, and D. Kleppner, "Nuclear polarization of spin-polarized hydrogen," *Physical Review Letters*, vol. 47, p. 1195, 1981. $E_B = 1.01$ K.

[49] H. P. Godfried, E. R. Eliel, J. G. Brisson, J. D. Gillaspy, C. Mallardeau, J. C. Mester, and I. F. Silvera, "Interaction of atomic hydrogen with undersaturated helium films," *Physical Review Letters*, vol. 55, p. 1311, 1985. $E_B = 0.96$ K.

[50] D. A. Bell, H. F. Hess, G. P. Kochanski, S. Buchman, L. Pollack, Y. M. Xiao, D. Kleppner, and T. J. Greytak, "Relaxation and recombination in spin-polarized atomic hydrogen," *Physical Review B*, vol. 34, p. 7670, 1986. $E_B = 1.04$ K.

[51] I. A. Yu, J. M. Doyle, J. C. Sandberg, C. L. Cesar, D. Kleppner, and T. J. Greytak, "Evidence for universal quantum reflection of hydrogen from liquid ⁴He," accepted by *Physical Review Letters*.